TRIBHUVAN UNIVERSITY
INSTITUTE OF ENGINEERING
PULCHOWK CAMPUS

NUMERICAL AND EXPERIMENTAL STUDY OF FLUIDIC THRUST VECTORING IN A CONVERGING-DIVERGING NOZZLE USING SHOCK VECTOR CONTROL

By:
Osika Shakya (077/BAS/027)
Rashu Kunwar (077/BAS/032)
Shreyas Shrestha (077/BAS/041)
Swikriti Puri (077/BAS/046)

A FINAL REPORT TO THE DEPARTMENT OF MECHANICAL AND AEROSPACE ENGINEERING IN PARTIAL FULFILLMENT OF THE REQUIREMENT FOR THE BACHELOR'S DEGREE IN AEROSPACE ENGINEERING

DEPARTMENT OF MECHANICAL AND AEROSPACE ENGINEERING
LALITPUR, NEPAL

March, 2025

COPYRIGHT

TRIBHUVAN UNIVERSITY

INSTITUTE OF ENGINEERING

PULCHOWK CAMPUS

DEPARTMENT OF MECHANICAL AND AEROSPACE ENGINEERING

LETTER OF APPROVAL

The undersigned certify that they have read, and recommended to the Institute of Engineering for acceptance, a project report entitled "**Numerical and Experimental Study of Fluidic Thrust Vectoring in a Converging-Diverging Nozzle using Shock Vector Control**" submitted by **Osika Shakya, Rashu Kunwar, Shreyas Shrestha and Swikriti Puri** in partial fulfilment of the requirements for the Bachelor's Degree in Aerospace Engineering.

Supervisor: **Asst. Prof. Kamal Darlami**

Department of Mechanical and Aerospace Engineering

Institute of Engineering, Pulchowk Campus

External Examiner: **Er. Sandip Gewali**

Tribhuvan University
Institute of Engineering
Department of Mechanical and Aerospace Engineering
Pulchowk Campus

Head of Department: **Asst. Prof. Dr. Sudip Bhattrai**

Department of Mechanical and Aerospace Engineering

Institute of Engineering, Pulchowk Campus

Date: March 9, 2025

ACKNOWLEDGEMENT

We would like to express our sincere appreciation to our supervisor, **Asst. Prof. Kamal Darlami**, for his constant guidance, motivation, and invaluable support throughout the course of this project. His supervision and insightful suggestions have been instrumental in shaping the project and helping us overcome numerous challenges along the way.

We extend our deepest gratitude to **Asst. Prof. Dr. Sudip Bhattrai**, Head of the Department of Mechanical and Aerospace Engineering, for his valuable insights, constant encouragement, and constructive feedback, all of which greatly contributed to the successful completion of this project. We would also like to thank our project co-ordinator, **Asst. Prof. Biman Rimal**, for his support and guidance throughout the project.

Our sincerest gratitude goes to our mentor, **Er. Salim Maharjan**, for his unwavering support and wise counsel from the very beginning of this project. His expertise in Schlieren imaging, along with his teachings and continuous feedback at every step, has played a crucial role in the successful completion of this project.

We would also like to thank the **Department of Mechanical and Aerospace Engineering, Institute of Engineering, Pulchowk Campus**, for providing us with this valuable opportunity to apply our academic knowledge to a practical project, significantly enriching our problem-solving skills. Our gratitude further extends to the **Incubation, Innovation, and Entrepreneurship Center (IIEC)**, Pulchowk Campus, for providing the necessary resources and workspace for our experimental setup and tests.

Finally, we are thankful to our families, friends, juniors, and seniors who have directly and indirectly supported us throughout this project. We sincerely welcome any feedback and suggestions that could help improve this project further.

Authors:
Osika Shakya
Rashu Kunwar
Shreyas Shrestha
Swikriti Puri

ABSTRACT

Fluidic thrust vectoring via Shock Vector Control (SVC) offers an efficient alternative to traditional mechanical systems by utilizing secondary flow injection to deflect primary supersonic jet exhaust. This study aims to investigate the effect of SVC on deflection of flow in a converging-diverging nozzle through numerical simulations and experimental testing. Simulations were conducted using ANSYS Fluent with varying Nozzle Pressure Ratios (NPR) and Secondary Pressure Ratios (SPR), while experimental tests employed a 3D-printed nozzle and Z-type Schlieren flow visualization. The experimental and numerical simulations were conducted for Mach 1.4 and Mach 1.6 nozzles at NPR values of 5, 6, and 7, with secondary pressures ranging from 1 bar to the respective primary pressure. Experimental results showed maximum deflection angle of 7.449 degrees, obtained at SPR 1 and NPR 6 at Mach 1.6 whereas minimum deflection of -0.803 was obtained at SPR 0.143 and NPR 7 at Mach 1.4. Similarly, simulation results showed maximum deflection of 6.185 at SPR 1 and NPR 5 at Mach 1.4 and minimum deflection of -0.638 was obtained at SPR 0.167 and NPR 6 at Mach 1.4. The research concluded effective thrust vectoring at higher SPR and higher Mach number.

Keywords: Converging-Diverging Nozzle, Flow Visualization, Fluidic Thrust Vectoring, Shock Vector Control, Supersonic Jets, Z-Type Schlieren

TABLE OF CONTENTS

TITLE PAGE i
COPYRIGHT ii
ACKNOWLEDGEMENT iii
ABSTRACT iv
TABLE OF CONTENTS vii
LIST OF FIGURES ix
LIST OF TABLES x
LIST OF ABBREVIATIONS xi
SYMBOLS xii

1 INTRODUCTION 1
1.1 Background 1
1.2 Problem Statement 2
1.3 Objectives 2
1.3.1 Main Objective 2
1.3.2 Specific Objectives 2
1.4 Applications 2
1.5 Feasibility Analysis 3
1.5.1 Economic Feasibility 3
1.5.2 Technical Feasibility 3
1.5.3 Operational Feasibility 3
1.6 System Requirements 3
1.6.1 Hardware Requirements 3
1.6.2 Software Requirements 4

2 LITERATURE REVIEW 5
2.1 History 5
2.2 Evolution of Fluidic Thrust Vectoring 5
2.3 Comparison Among the FTV techniques 7
2.4 Governing Theories 8
2.4.1 Converging Diverging (CD) Nozzle 8
2.4.2 Area - Mach Relation 9
2.4.3 Underexpanded and Overexpanded Nozzle 10
2.4.4 Shock Vector Control (SVC) Method 11
2.4.5 Z-type Schlieren Imaging 12

3 METHODOLOGY 14
3.1 Nozzle Design 15

3.1.1 Selection of design parameters . . . 15
3.1.2 Inlet Conditions . . . 15
3.1.3 Throat Conditions . . . 16
3.1.4 Outlet Conditions . . . 16
3.1.5 Nozzle Geometry . . . 17
3.2 Numerical Simulation . . . 18
3.2.1 Meshing . . . 19
3.2.2 Mesh Independence Study . . . 20
3.2.3 Setup and Solution . . . 21
3.3 Experimental Setup . . . 23
3.3.1 CAD Model . . . 23
3.3.2 Material selection and fabrication . . . 24
3.3.3 Thrust Vectoring Setup . . . 25
3.3.4 Flow Visualization . . . 27
3.4 Post Processing . . . 29
3.4.1 Simulation Post Processing . . . 29
3.4.2 Experimental Post Processing . . . 31

4 RESULT AND DISCUSSIONS 33
4.1 Output . . . 33
4.1.1 Numerical Simulation Results . . . 33
4.1.2 Experimental Results . . . 36
4.2 Result Analysis . . . 40
4.2.1 Data Collection . . . 40
4.2.2 Evaluation of Plot . . . 43
4.2.3 Evaluation of Results Based on First Shock Diamond Distance . 44
4.2.4 Comparison of Experimental and Simulation Results . . . 45
4.3 Work Completed . . . 46
4.4 Limitations . . . 47
4.5 Problems Faced . . . 47
4.6 Budget Analysis . . . 47

5 CONCLUSION AND FUTURE ENHANCEMENT 49
5.1 Conclusion . . . 49
5.2 Scope for Future Enhancement . . . 49
REFERENCES . . . 51
APPENDIX . . . I
A APPENDIX I . . . I
A.1 MOC CONTOUR . . . I

A.2 2D SKETCH II
A.3 3D GEOMETRY III
A.4 3D Mesh IV
A.5 EXPERIMENTAL COMPONENTS V
A.6 MOC CODE VI

LIST OF FIGURES

2.2.1 Evolution of fluidic thrust vectoring controls techniques 6
2.4.1 Flow through a Converging-Diverging (CD) Nozzle 8
2.4.2 Variation of Mach Number with area ratio 9
2.4.3 Underexpanded nozzle 10
2.4.4 Overexpanded nozzle 11
2.4.5 Side view of 2D CD nozzle using shock vector control to produce pitch thrust vectoring 11
2.4.6 Schematic diagram of Z-type Schlieren method[1] 13

3.0.1 Flowchart of Methodology 14
3.1.1 2D sketch of nozzle for Mach 1.4 with secondary inlet 18
3.2.1 Mesh of nozzle with flow domain for Mach 1.4 19
3.2.2 Zoomed mesh at various region for Mach 1.4 20
3.2.3 Boundary Conditions for Mach 1.4 22
3.2.4 Boundary Conditions for Mach 1.4 with secondary 23
3.3.1 3D geometry for Mach 1.4 24
3.3.2 3D geometry with secondary inlet for Mach 1.4 24
3.3.3 3D printed nozzle without and with secondary inlet 25
3.3.4 Schematic Drawing of the Experimental Setup 26
3.3.5 Flow Control Circuit 27
3.3.6 Z-Type Schlieren Setup[1] 28
3.3.7 Full Experimental Setup 29
3.4.1 Angle Measurement using density contour for Mach 1.4 at NPR 5 and Secondary Pressure 5 bar 30
3.4.2 Distance Measurement using density contour for Mach 1.4 at NPR 5 and Secondary Pressure 5 bar 31
3.4.3 Angle Measurement of Experimental Picture obtained for Mach 1.4 NPR 6 Secondary Pressure 2 bar 31
3.4.4 Distance Measurement of Experimental Picture obtained for Mach 1.4 NPR 6 Secondary Pressure 2 bar 32

4.1.1 Velocity Contours without secondary inlet for Mach 1.4 34
4.1.2 Velocity Contours at NPR 5 for various Secondary Pressure for Mach 1.4 34
4.1.3 Velocity Contours at NPR 6 for various Secondary Pressure for Mach 1.4 34
4.1.4 Velocity Contours at NPR 7 for various Secondary Pressure for Mach 1.4 35
4.1.5 Velocity Contours without secondary inlet for Mach 1.6 35

4.1.6 Velocity Contours at NPR 5 for various Secondary Pressure for Mach 1.6 35
4.1.7 Velocity Contours at NPR 6 for various Secondary Pressure for Mach 1.6 36
4.1.8 Velocity Contours at NPR 7 for various Secondary Pressure for Mach 1.6 36
4.1.9 Schlieren Images without secondary inlet for Mach 1.4 37
4.1.10 Schlieren Images at NPR 5 for various Secondary Pressure for Mach 1.4 37
4.1.11 Schlieren Images at NPR 6 for various Secondary Pressure for Mach 1.4 37
4.1.12 Schlieren Images at NPR 7 for various Secondary Pressure for Mach 1.4 38
4.1.13 Schlieren Images without secondary inlet for Mach 1.6 38
4.1.14 Schlieren Images at NPR 5 for various Secondary Pressure for Mach 1.6 39
4.1.15 Schlieren Images at NPR 6 for various Secondary Pressure for Mach 1.6 39
4.1.16 Schlieren Images at NPR 7 for various Secondary Pressure for Mach 1.6 40
4.2.1 Secondary Pressure Vs Deflection angle for various NPR at Mach 1.4 . 43
4.2.2 Secondary Pressure Vs Deflection angle for various NPR at Mach 1.6 . 43
4.2.3 Secondary Pressure Vs Experimental Deflection angle for Mach 1.4 and Mach 1.6 at various NPR 44
4.2.4 SPR Vs Distance of first shock diamond from outlet of nozzle for Mach 1.4 45
4.2.5 SPR Vs Distance of first shock diamond from outlet of nozzle for Mach 1.6 45
4.2.6 SPR Vs Deflection for experimental and simulation results at Mach 1.4 46
4.2.7 SPR Vs Deflection for experimental and simulation results at Mach 1.6 46

A.1 Diverging section contour using MOC I
A.2 Diverging section nozzle I
A.3 2D sketch of nozzle without secondary injection for Mach 1.4 II
A.4 2D sketch of nozzle without secondary injection for Mach 1.6 II
A.5 2D sketch of nozzle with secondary injection for Mach 1.6 III
A.6 3D geometry for Mach 1.6 III
A.7 3D geometry with secondary injection for Mach 1.6 IV
A.8 3D mesh of nozzle for Mach 1.6 IV
A.9 Zoomed section of 3D mesh of nozzle for Mach 1.6 V
A.10 Valves V
A.11 Gorilla Tripod Stand VI
A.12 Sony ZV-E10 Mirrorless Camera VI

LIST OF TABLES

3.1.1 Inlet parameters 16
3.1.2 Throat parameters 16
3.1.3 Outlet parameters 17
3.1.4 Dimensions of geometry 17
3.2.1 Mesh Independence Study 21
3.2.2 Setup and solutions parameters 22

4.2.1 Deflection Angle 42
4.6.1 Budget Table 48

LIST OF ABBREVIATIONS

2D	2-Dimensional
3D	3-Dimensional
AC	Alternating Current
AUSM	Advection Upstream Splitting Method
BDTN	Bypass Dual Throat Nozzle
CAD	Computer Aided Design
CD	Converging-Diverging
CFD	Computational Fluid Dynamics
DC	Direct Current
DMAE	Department of Mechanical and Aerospace Engineering
DOE	Design Of Experiments
DTN	Dual Throat Nozzle
FTV	Fluidic Thrust Vectoring
HP	Horse Power
LED	Light Emitting Diode
MATLAB	MATrix LABoratory
MOC	Method Of Characteristics
MTV	Mechanical Thrust Vectoring
NASA	National Aeronautics and Space Administration
NPR	Nozzle Pressure Ratio
PLA	Polylactic acid
SPR	Secondary Pressure Ratio
STL	Stereolithography
STOL	Short Take-Off and Landing
SVC	Shock Vector Control
TS	Throat Shifting
TV	Thrust Vectoring
TVC	Thrust Vectoring Control
USS	United States Ship
U.S.	United States
VTOL	Vertical Take-Off and Landing

SYMBOLS

A	Area
A^*	Throat Area
A_e	Exit Area
a_e	Speed of sound at exit
M	Mach number
M_e	Exit Mach number
P_a	Ambient Pressure
P_c	Chamber Pressure
P_e	Exit Pressure
P_t	Throat Pressure
T_c	Chamber Temperature
T_e	Exit Temperature
T_t	Throat Temperature
ρ_c	Chamber Density
ρ_e	Exit Density
ρ_t	Throat Density
$\theta_{withoutsecondary}$	Deflection angle without secondary inlet
$\theta_{withsecondary}$	Deflection angle with secondary inlet
$\theta_{deflection}$	Net deflection angle
u	x direction velocity
v	y direction velocity
W	Weight
γ	ratio of specific heat of gas

CHAPTER 1:
INTRODUCTION

1.1. Background

Enhancement in the aerospace power with thrust vectoring innovation has improved the maneuverability, control effectiveness, health, performance and stealth. “Thrust vectoring provides such a significant advantage in the visual maneuvering arena that I rarely find myself in a defensive position,” says Wagemann. “When we start defensive, for training, you are almost always able to transition to offensive without getting shot.” Thrust vectoring technology has redefined the traditional aircraft exhaust design[2]. Mainly, there are two methods of thrust vectoring, namely mechanical thrust vectoring(MTV) and fluidic thrust vectoring(FTV). Mechanical thrust vectoring method deflects the direction of primary flow by the use of actuators and gimbaling mechanisms whereas fluidic thrust vector is such a method of achieving such deflection/ deviation in the exhaust flow by introducing secondary flow into the primary flow.

Detailed experimental and numerical efforts have been made to predict the impinging masses that lead to successful fluidic thrust vectoring-launching[3]. NASA Langley Research Center have tested both experimentally and computationally for 3 methods of fluidic thrust vectoring: Shock Vector Control (SVC) method, Throat Shifting (TS) method and the counter flow method which concluded with a result of having best thrust efficiency in throat shifting method and larger thrust vectoring angle with shock vector control method [4]. FTV is more desirable due to its quick integration into existing systems [5][6].

This research aims to study the flow phenomenon at the exhaust nozzle while diverting the primary flow with secondary flow at diverging section of CD nozzle and investigating the thrust vectoring technique. The analysis of fluidic thrust vectoring will be conducted for a method under the domain of supersonic nozzle, namely Shock vector control. The vectored flow from the CD nozzle would be analyzed with the numerical methods of simulation and experimental optical flow visualization technique, i.e. schlieren flow visualization technique. The results would then be compared to get an insight on the effectiveness of fluidic thrust vectoring technique.

1.2. Problem Statement

Flow injection in diverging section of nozzle was explored and many research have been progressing for greater thrust vectoring performance. MTV technique is a mature technique and has been widely used TV method in aircrafts [7]. However, application of MTV technique in aircraft comes with the limitations of increased weight, complex design and expensive in cost. Therefore, various fluidic thrust vectoring techniques have been developed and the research is continually evolving to overcome these shortcomings of the MTV technique. Thus, research and study needs to be conducted to improve the effectiveness of the thrust vectoring method for supersonic jets. This project aims to investigate the effect of secondary flow injection in the primary flow in a CD nozzle which will help in development of the solution for increasing effectiveness of vectored thrust and overcome the limitations of MTV.

1.3. Objectives

1.3.1. Main Objective

The primary objective of this project is to investigate the effect of fluidic thrust vectoring in CD nozzle for supersonic jet using shock vector control.

1.3.2. Specific Objectives

1. To reform an experimental setup for secondary flow injection.

2. To design a CD nozzle with secondary flow injector at diverging section.

3. To carry out the experimental tests and numerical simulation.

4. To compare the result from experiment and the numerical simulation.

5. To investigate the thrust vectoring with varying NPR and SPR.

1.4. Applications

1. FTV technique can be used for quicker rotation and lift-off of an aircraft, even at lower speeds.

2. Vectoring of thrust can be applicable in an aircraft for a lower deflection of the

aerodynamic control surfaces so reducing drag and radar cross section and increasing maneuverability potential[8].

3. FTV is useful for achieving the same vectoring control as MTV but with 50% reduced weight, cost and complexity of the system.

1.5. Feasibility Analysis

1.5.1. Economic Feasibility

The estimation of the cost for the reformation of the set up incorporating the injection of secondary flow with pump or compressor is approximately Rs. 25,000. The cost in accordance to the outcome of the project extracted is quite feasible economically.

1.5.2. Technical Feasibility

The accessibility of the required software for the design of CD-nozzle, 3D printing facility, software to perform numerical simulation of flow inside the CD-nozzle and availability of optical flow visualization techniques like z-type schlieren setup ensures this project's technical feasibility. The manpower and tools required for the reformation of high compressor setup have been carefully evaluated for the completion of the project in an efficient way.

1.5.3. Operational Feasibility

The timeframe for the completion of the project has been systematically distributed that makes sure of the completion of all the work before deadline. The proper project planning, understanding the aspects of the project, identification of the obstacles during this project makes it operationally feasible.

1.6. System Requirements

1.6.1. Hardware Requirements

1. Thrust Vectoring Setup

2. Z- Type Schlieren setup

3. 3D printer

1.6.2. Software Requirements

1. ANSYS
2. SOLIDWORKS
3. MATLAB
4. POINTWISE
5. ImageJ
6. GIMP

CHAPTER 2:
LITERATURE REVIEW

2.1. History

The concept of Thrust Vectoring Control(TVC) dates back to the 1930s when Robert Goddard used exhaust vanes and gimbaled engines in rocketry and ballistic missiles for attitude control outside the atmosphere. Fluidic injection for throttling and vectoring was explored in the 1950s, in order to use in rocket nozzle systems, which controlled the primary flow deflection by penetrating the secondary fluid into the divergent section of the rocket nozzle[9]. The British Army airship Delta first used Mechanical Thrust Vectoring(MTV) for control, followed by the British rigid airship HMA No. 9r and the U.S. Navy rigid airships USS Akron and USS Macon. Thrust vectoring was originally enforced to provide upward vertical thrust for aircraft's (VTOL) or short(STOL) takeoff and landing ability. Flight tests of thrust-vectoring designs began in the early 1990s with airplanes like NASA's modified F/A-18 and F-15, the Rockwell/MBB X-31, and a modified Air Force F-16[10]. In May 1983, Pratt & Whitney designed F119 for Lockheed Martin F-22 Raptor, an after-burning turbofan engine which incorporates a 2D rectangular CD nozzle enabling the aircraft to deflect the engine thrust at roughly 20 degrees in pitch axis enhancing maneuverability[11].

The potential use of FTV in aerospace applications remained under-explored until the 1990s. Renewed interest in FTV emerged due to its ability to achieve better control and performance comparable to MTV but with reduced weight and cost. The research concluded that FTV was capable of achieving the same vectoring control as MTV but with 50% reduced weight and cost[12]. The concept of FTV involves deflecting the thrust of a jet engine by using the influence of a secondary jet. This secondary flow is typically injected into or near the primary jet exhaust, which changes the line of thrust with few, or any, moving parts, hence reducing the weight and complexity of the nozzle.

2.2. Evolution of Fluidic Thrust Vectoring

The development of FTV techniques has evolved significantly over the decades, offering innovative methods for controlling thrust in an efficient manner as shown in figure 2.2.1.

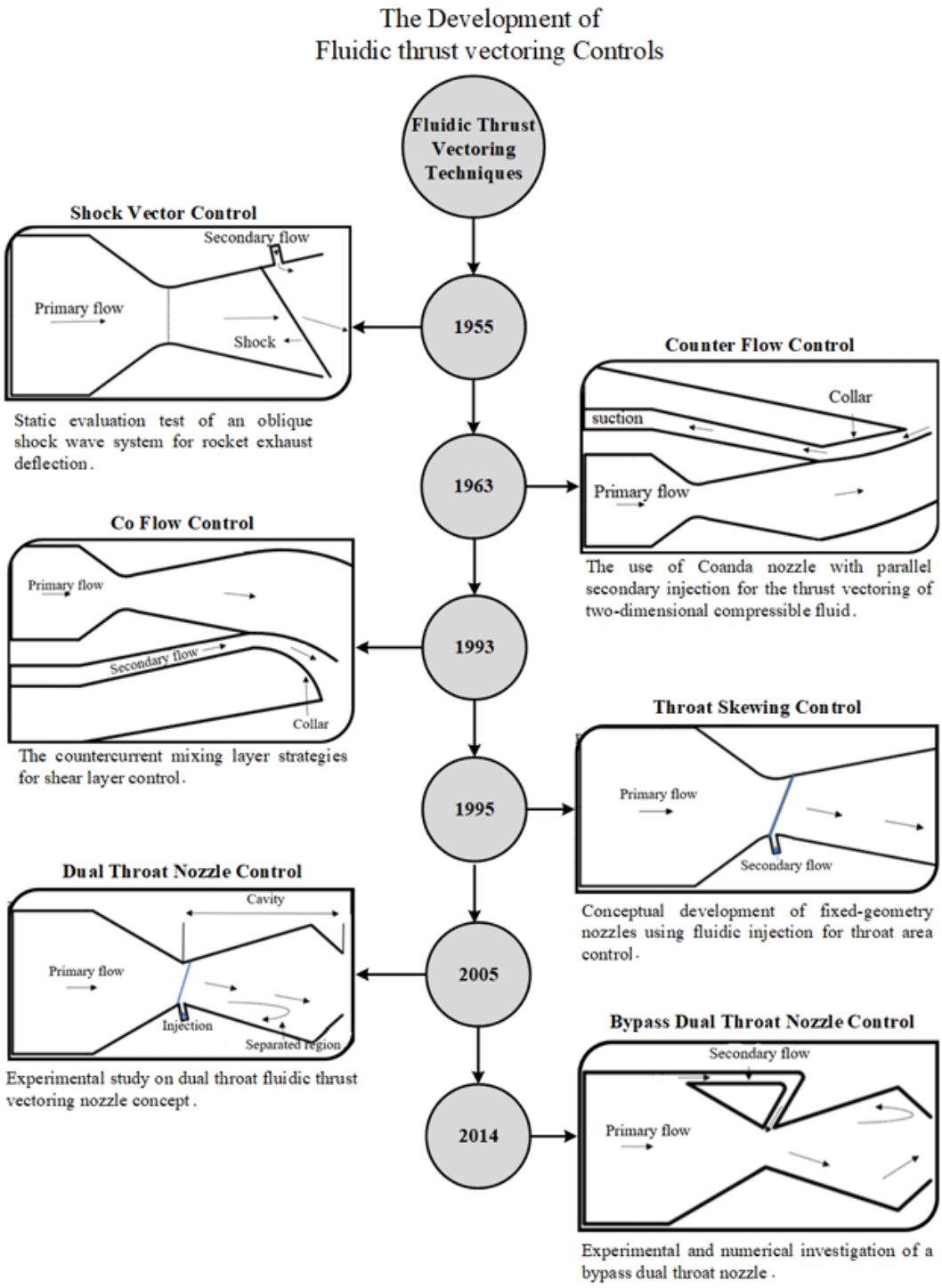

Figure 2.2.1: Evolution of fluidic thrust vectoring controls techniques [13]

According to Kowal, the journey began in 1955 with Shock Vector Control, which utilized oblique shock waves for exhaust deflection through secondary and primary flow interactions at the diverging section[13][14]. By 1963, the Counter Flow Control approach emerged,making use of the Coanda effect (tendency of a fluid to stick to a curved

surface), in which thrust vectoring is achieved by passing the secondary air stream in the opposite direction of primary flow[15]. Advancements in 1993 introduced Co Flow Control which also makes use of the Coanda surface as that of counter flow method. In this, Coanda surface is positioned at the exit of the nozzle and the secondary stream of co-flowing air is introduced parallel to the Coanda surface in tangential direction due to which the primary flow gets diverted in the direction of secondary flow[16]. This progress was furthered in 1995 with Throat Skewing Control, which uses secondary fluidic injection at a throat region in such a way so as to shift the throat from geometrically minimum area to aerodynamically minimum skewed region to achieve vector control[17]. A significant experimental milestone occurred in 2005 with the Dual Throat Nozzle (DTN) Control, where thrust vectoring was achieved via secondary normal injection around throat and asymmetric secondary injection at the diverging section[18]. With the ever-growing interest in improving the FTV techniques, recently, in 2014, the Bypass Dual Throat Nozzle (BDTN) Control came into existence,which is an extension of conventional DTN that demonstrates refined thrust vectoring capabilities via bypass secondary flows with a greater efficiencies than other FTV methods[19].

2.3. Comparison Among the FTV techniques

So far, numerous studies and researches have been done on all of the aforementioned FTV techniques. A preliminary comparison of the techniques draws out the performance, efficiencies, vectoring capabilities, advantages and limitations of each of the method. In an experiment conducted by [14], it was found that the co-flow method was unsuccessful, to which the paper concluded:it might have been due to the high aspect ratio of the nozzle whilst, significant pitch thrust vectoring angles (approximately 10° to 20°) were achieved via SVC. Computational and experimental investigations were conducted by Abdullah for the co-flow method, which showed that the increase in secondary jet mass flow rate increases the jet vectoring angle[15]. In a research conducted by [17], where the concept of fluidic throat skewing was developed using computational fluid dynamics (CFD) and a design of experiments (DOE), it was found that, the thrust efficiency is approximately 5% higher than the SVC approach, with roughly 1.5 degrees of vectoring for every 1% of injected flow . To improve the vectoring effect of the throat skewing method, [18] designed and tested a dual throat nozzle in the NASA Langley Research Center Jet Exit Test Facility, concluding that, this nozzle had a greater thrust efficiencies than any other FTV techniques, only for this statement to be changed later. Research shows that for the same value of NPR, BDTN achieves greater deflection angle than the DTN method [19]. Existing literature indicates that shock vector control performs well in terms of thrust vectoring angle. The only drawback is the shock im-

pingement on the opposite wall of the nozzle and hence the thrust losses. So, the main focus of this project is to achieve thrust vectoring via shock vector control.

2.4. Governing Theories

2.4.1. Converging Diverging (CD) Nozzle

A CD nozzle, also called de-Laval nozzle is a special type of nozzle that is formed by combining both the converging (inlet area is greater than the exit area) and diverging nozzle (inlet area is lesser than the exit area) in such a way that the flow achieves a sonic speed at throat. As flow passes through the converging section, Mach number increases and ultimately reaches to sonic at throat (geometrically minimum area). Whether the flow reaches sonic or supersonic speed, depends upon the ratio of inlet area to the throat area. This is given by the Area-Velocity relation, which is given as following:

$$\frac{dA}{A} = \frac{dV}{V}(M^2 - 1)$$

This tells that for M = 1(sonic) or $M < 1$(subsonic), area and velocity have inverse relation and for $M > 1$ (supersonic), area and velocity have direct relation as shown in figure[2.4.1].

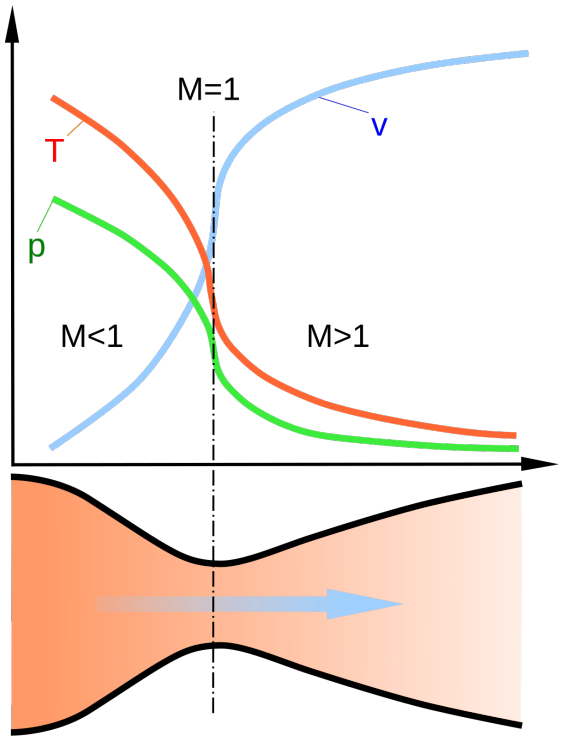

Figure 2.4.1: Flow through a Converging-Diverging (CD) Nozzle [15]

From the above, it can be seen that velocity increases from subsonic in convergent section to sonic at throat becoming supersonic towards the divergent section. However, at the inlet of the nozzle, the static pressure and temperature is maximum which decreases as the fluid moves from inlet towards throat and the exit. We consider that the flow in the nozzle is isentropic, thus total pressure and total temperature remains constant throughout. However, due to irreversiblity caused by friction, isentropic condition is unachievable. And as a result, the total exit pressure is actually lesser than the total pressure at the inlet. There are no moving parts and no work is imparted nor any work is done by or on the fluid during the entire process and thus there is no change in total temperature. However, leakage, heat conduction etc through the parts will cause decrease in the total temperature. Similarly, this process is considered as adiabatic process as there is neither exchange nor addition of energy during the flow and the corresponding expansion is considered as an adiabatic expansion[20].

2.4.2. Area - Mach Relation

Using the continuity and isentropic relations, area-mach relation can be derived which is shown below:

$$\frac{A}{A^*} = \frac{1}{M}\left(\frac{2}{\gamma+1}\left(1+\frac{\gamma-1}{2}M^2\right)\right)^{\frac{\gamma+1}{2(\gamma-1)}}$$

This equation tells that at any location, mach number is a function of ratio of local duct area to sonic throat area. There are two values of M for any given area ratio, subsonic and supersonic as shown in figure 2.4.2[20].

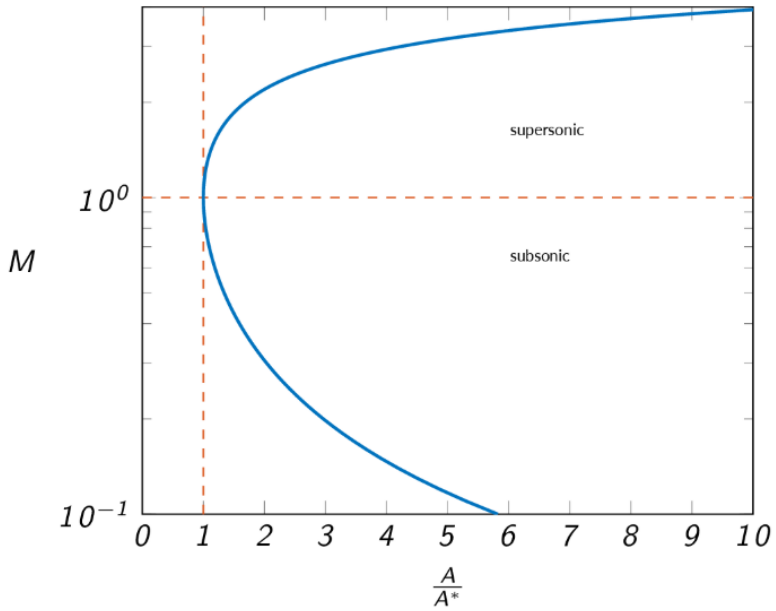

Figure 2.4.2: Variation of Mach Number with area ratio [21]

2.4.3. Underexpanded and Overexpanded Nozzle

An underexpanded nozzle occurs when the exit pressure (Pe) is greater than the back pressure (Pb). To maintain the pressure equilibrium, the jet undergoes a supersonic expansion process as described by Prandtl-Meyer flow, creating expansion waves at the jet boundary. The centerline symmetry condition requires the flow to remain parallel to the centerline, leading to additional expansion fans that result in regions of pressure below the back pressure. Consequently, a cyclic wave pattern of expansion and compression waves forms, leading to a jet with alternating regions of decreasing and increasing pressure as shown in figure 2.4.3. In an inviscid (ideal) flow, this process would repeat indefinitely; however, in reality, viscous losses and turbulent mixing dampen the wave pattern after a few cycles[22].

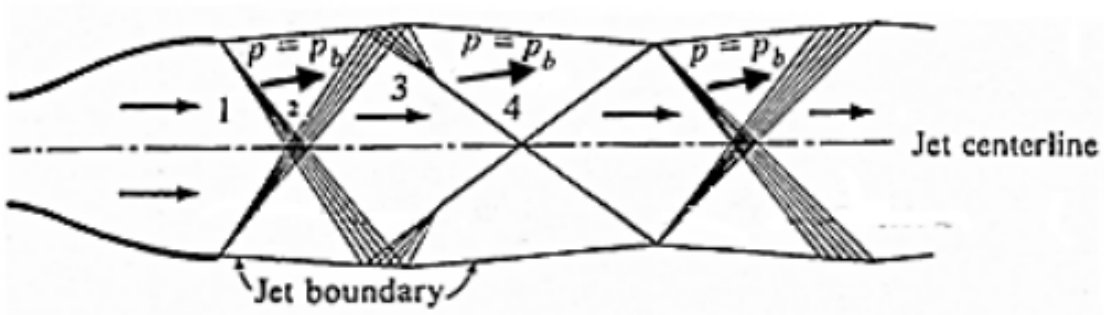

Figure 2.4.3: Underexpanded nozzle
[22]

An overexpanded nozzle occurs when the back pressure (Pb) is greater than the exit pressure (Pe). In order to match the higher back pressure, the jet undergoes a supersonic compression process through oblique shocks at the jet boundary, causing the flow to turn inward and the pressure to rise. Similar to the underexpanded case, the centerline condition ensures reflected shocks occur, balancing the symmetry of the flow. These shocks result in a cyclic pattern where compression waves are followed by expansions fans, forming regions of increasing and decreasing pressure as shown in figure 2.4.4. This wave pattern appears out-of-phase compared to an underexpanded nozzle, as compression waves occur first. The overexpanded flow creates observable Mach diamonds, where regions of high pressure, density, and temperature appear, sometimes visible as bright spots in high-temperature jets[22].

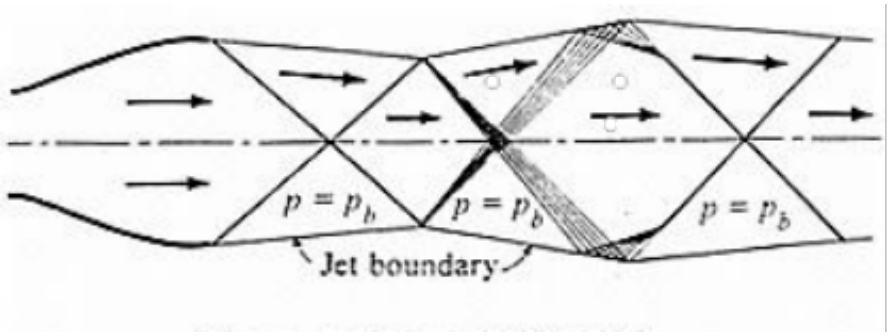

Figure 2.4.4: Overexpanded nozzle
[22]

2.4.4. Shock Vector Control (SVC) Method

Fluidic thrust vectoring using the shock vector control method involves deflecting the primary jet exhaust in the pitch direction by utilizing an oblique shock wave generated in the divergent region as described in figure 2.4.5. As the supersonic flow in the diverging section of the nozzle encounters the secondary airflow, it creates an oblique shock wave that deflects the primary jet exhaust, thereby changing the direction of thrust in the direction of the secondary flow injection without the need for mechanical components[4].

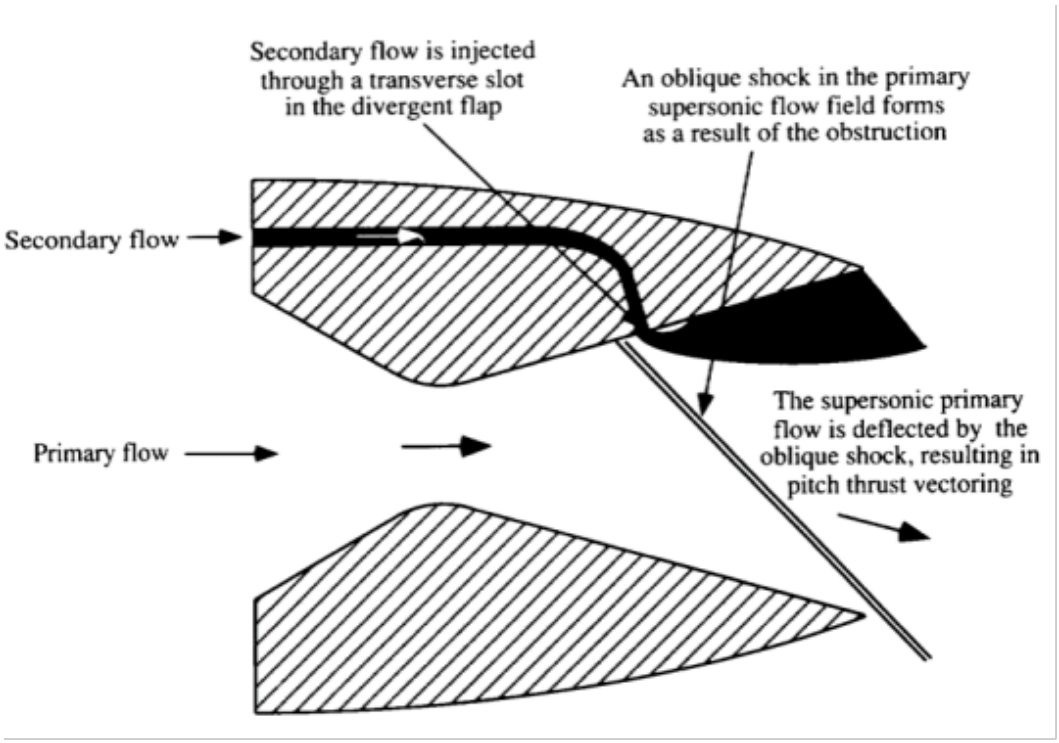

Figure 2.4.5: Side view of 2D CD nozzle using shock vector control to produce pitch thrust vectoring
[4]

The vectoring angle is influenced by mass flow ratio, injector location, injector design, and secondary injection angle. An investigation conducted in the Langley Research Center varying NPR from 2 to 10 and secondary weight flow from 0 to 10 percent of the primary weight flow, concluded that the larger angle of deviation were achieved at lower values of NPR. Increasing the secondary injection flow rate had a positive effect on vectoring angle. Impingement of the oblique sock on the opposite divergent flap caused the vectoring angle to decrease although the secondary flow ratio was increased. However, increasing the secondary flow ratio increased the impingement location further upstream[4]. Similar results were obtained by A.S N who varied the mass flow ratio by varying the stagnation pressure ratios[23].

2.4.5. Z-type Schlieren Imaging

Schlieren imaging is one of the optical techniques used to visualize fluid density changes in transparent media. It is a non-intrusive technique, particularly useful in high speed flows in which compressibility is an important factor causing the density changes. Among different configurations, the Z-type schlieren is the one of the most popular system implemented due to its compact design, high sensitivity and flexibility for different test sizes. It is advantageous for visualizing flows in CD nozzles, making it well suited for studying SVC technique, where the ability to observe the exhaust jet with shock patterns and flow behavior is essential.

The Z-type schlieren setup consists of two parabolic or spherical mirrors arranged in opposite directions relative to the optical axis. This configuration causes the light to travel in “Z” path, which explains its name [1]. A coherent point light source is placed at focal distance from the first mirror that illuminates it and supplies collimated beam of light onto second mirror passing through the test section in the middle. The second mirror refocuses the light onto a knife-edge or colored filter forming the image onto camera placed behind it. The knife-edge which is also located at focal distance from the second mirror is used to partially block the intensity of light such that sensitivity and contrast of the schlieren image can be adjusted as per requirement. Both the mirrors are tilted by a certain angle and separated by distance about twice the focal length of the identical mirrors. The schematic diagram for Z-type schlieren setup can be seen in the figure 2.4.6.

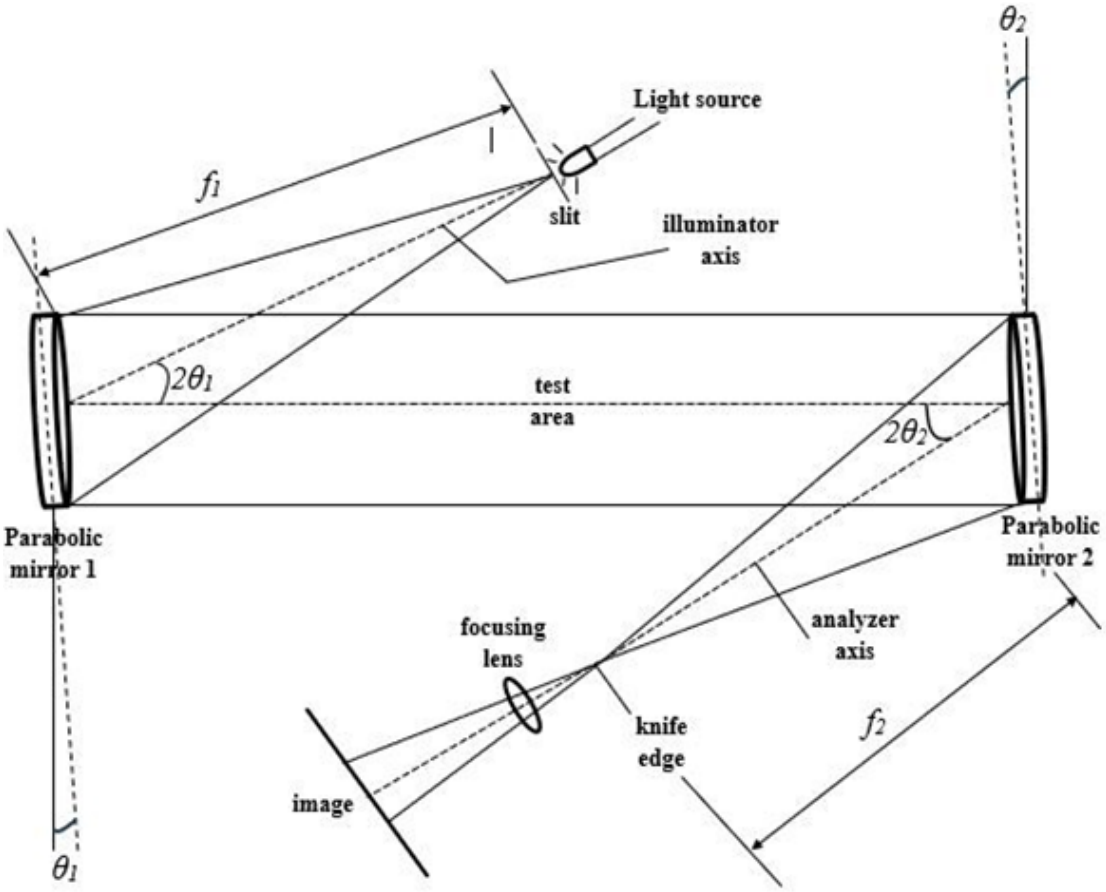

Figure 2.4.6: Schematic diagram of Z-type Schlieren method[1]

Although the Z-type schlieren is a versatile and great optical technique, it suffers from inherent issues such as comatic aberration and astigmatism. Coma or comatic aberration forms as elongation of point image into comet like streaks, causing the image quality to degrade. Astigmatism, a more persistent issue, is due to off-axis rotation of mirrors, causing a path difference in reflected light rays which results in two short line images and displaced along the optical axis. These issues cannot be completely eliminated but can be minimized by maintaining equal and small tilt angles and using higher focal length mirrors[1].

CHAPTER 3:
METHODOLOGY

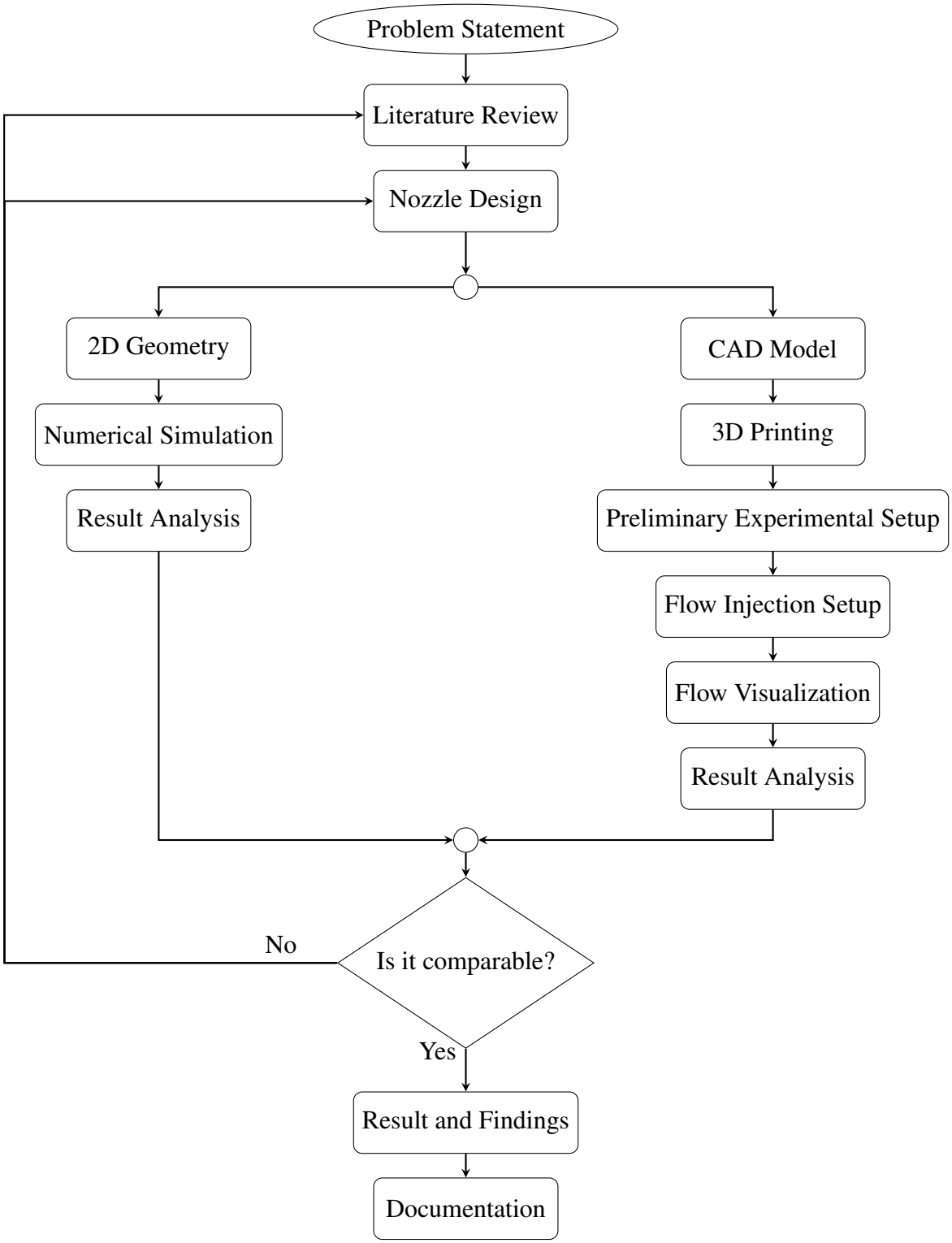

Figure 3.0.1: Flowchart of Methodology

3.1. Nozzle Design

A converging-diverging nozzle must be designed to facilitate the computational and experimental tests required to study fluidic thrust vectoring. The nozzle's design relies on a theoretical understanding of the physics governing converging-diverging nozzles and compressible supersonic flow[24].

By applying mathematical equations, including the isentropic pressure relation and the area-Mach number relation, the design and key thermodynamic parameters—such as pressure, temperature, and Mach number—will be determined for various sections of the nozzle.

3.1.1. Selection of design parameters

The design parameters for airflow through the nozzle are defined as follows:

- Specific heat ratio (γ) = 1.4
- Gas constant (R) = 287 J/(kg·K)
- Ambient pressure at the nozzle exit (P_a) = 101,325 Pa

The nozzle is designed for an exit Mach number of 1.4 and 1.6.

3.1.2. Inlet Conditions

The properties of the stagnant inlet chamber can be calculated using the relations provided below:

$$\frac{P_c}{P_a} = (1 + \frac{\gamma - 1}{2} M_e^2)^{\frac{\gamma}{\gamma - 1}}$$

$$\rho_c = \frac{P_c}{R * T_c}$$

For the optimum operation condition of nozzle, $P_e = P_a = 101325 Pascal$.

Table 3.1.1: Inlet parameters

Mach Number	Parameter	Values
1.4	Pressure(P_c) Temperature(T_c) Density(ρ_c)	322443.729 Pascal 300 K 3.745 kg/m^3
1.6	Pressure(P_c) Temperature(T_c) Density(ρ_c)	430673.234 Pascal 300 K 5.002 kg/m^3

3.1.3. Throat Conditions

The flow choke in the throat and becomes sonic which means that the mach number is equal to 1. Downstream the throat, nozzle diverges.

$$(1-M^2)\frac{dV}{V} = -\frac{dA}{A}$$

From the above equation, for supersonic flow, when the area increases, the velocity increases. The properties at the throat can be calculated using the relations provided below:

$$T_t = \frac{2T_c}{\gamma+1}$$

$$P_t = P_c(\frac{\gamma+1}{2})^{\frac{-\gamma}{\gamma-1}}$$

Table 3.1.2: Throat parameters

Mach Number	Parameter	Values
1.4	Pressure (P_t) Temperature (T_t)	170341.14 Pascal 250 K
1.6	Pressure(P_t) Temperature (T_t)	227516.826 Pascal 250 K

3.1.4. Outlet Conditions

The exit parameters can be calculated using the isentropic relations as follows:

$$\frac{T_c}{T_e} = (1+\frac{\gamma-1}{2}M_e^2)$$

$$\frac{P_c}{P_e} = (1+\frac{\gamma-1}{2}M_e^2)^{\frac{\gamma}{\gamma-1}}$$

$$\rho_e = \frac{P_e}{R * T_e}$$

Table 3.1.3: Outlet parameters

Mach Number	Parameter	Values
1.4	Pressure (P_e) Temperature (T_e) Density (ρ_e) Velocity of sound (a_e)=$\sqrt{\gamma * R * T_e}$	101325 Pascal 215.517 K 1.638 kg/m^3 294.269 m/s^2
1.6	Pressure(P_e) Temperature (T_e) Density (ρ_e) Velocity of sound (a_e)=$\sqrt{\gamma * R * T_e}$	101325 Pascal 198.41 K 1.779 kg/m^3 282.35 m/s^2

3.1.5. Nozzle Geometry

A planar nozzle has been taken for the project as it provides better flow visualization and the flow characteristics are uniformly distributed along the plane. The dimensions of the throat are taken arbitrarily and using the area-mach relation, the area of the exit of nozzle has been determined.

Table 3.1.4: Dimensions of geometry

Mach Number	Section	Width(mm)	Height(mm)	Area(mm)
1.4	Throat Exit	4 4	6 6.7	24 26.8
1.6	Throat Exit	4 4	6 7.5	24 30

The required mass flow rate for the flow to choke in the throat can be calculated using the following formula:
Mass flow rate = $A_e * \rho_e * v_e$
For mach 1.4, mass flow rate = 0.01858 kg/s
For mach 1.6, mass flow rate = 0.02411 kg/s

For the converging section of the nozzle, the diameter of the inlet is taken as 30mm (existing setup diameter). For designing the diverging section of the nozzle, the theory of MOC (Method of Characteristics) and the MATLAB tool have been used similar to the design of the CD nozzle by [24]. The contour of the diverging section is imported in solidworks and the 2D geometry for simulation and 3D geometry for the fabrication

has been created. The 2D sketch of the geometry with contour of diverging sections for mach 1.4 is shown in figure 3.1.1.

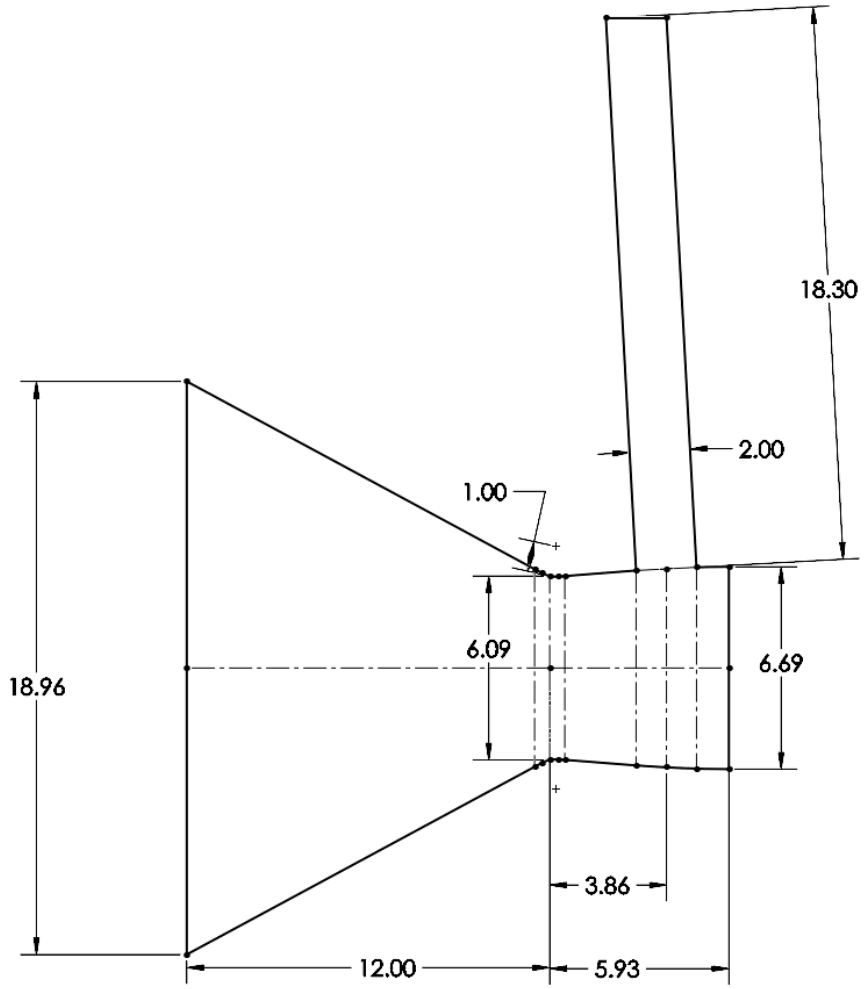

Figure 3.1.1: 2D sketch of nozzle for Mach 1.4 with secondary inlet

3.2. Numerical Simulation

ANSYS 2022 has been utilized for numerical CFD simulation of the flow in the nozzle and to observe fluid vectoring. ANSYS is a comprehensive simulation software widely used in various engineering fields for analyzing structures, thermal phenomena, fluid dynamics, and more. Within the ANSYS suite, ANSYS Fluent has been employed for this study. ANSYS Fluent is a computational fluid dynamics (CFD) software designed to simulate fluid flow, heat transfer, and chemical reactions under complex conditions. It provides a robust CFD solver with various turbulence models for conducting simulations effectively.

3.2.1. Meshing

Meshing is the crucial step for the CFD simulation that can affect greatly in quality of the result such as accuracy, efficiency and stability of the solutions. It discretizes the geometry into the smaller elements. A fine mesh in areas with high gradients captures the more detailed physics. The 2D geometry created using solidworks was imported as a database in the POINTWISE software for meshing in Initial Graphics Exchange Specification (.iges) file format. Pointwise is the advanced meshing tool for creating high quality meshes used in CFD. The geometry was divided into the smaller section and the connectors were generated. The boundary conditions were specified as pressure inlet, pressure outlet, walls and symmetry. The number of divisions on each edges was fed such that the mesh quality was fine and can capture the flow properly. The mesh quality on various sections of the geometry is shown in figure 3.2.1 and figure 3.2.2.

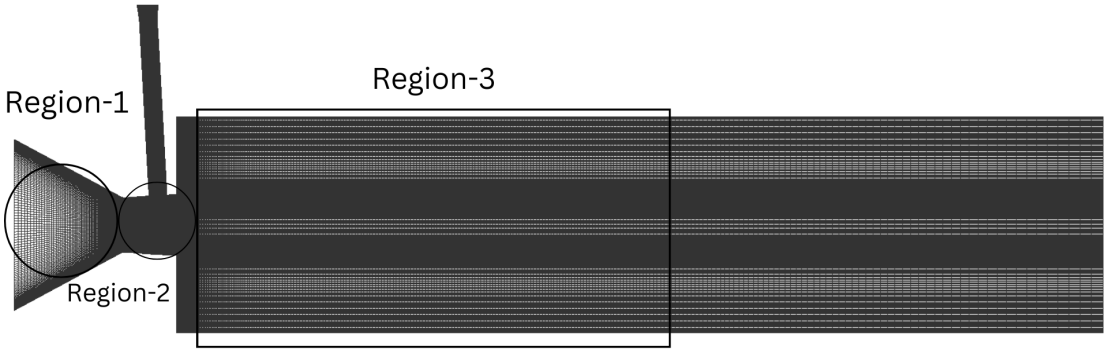

Figure 3.2.1: Mesh of nozzle with flow domain for Mach 1.4

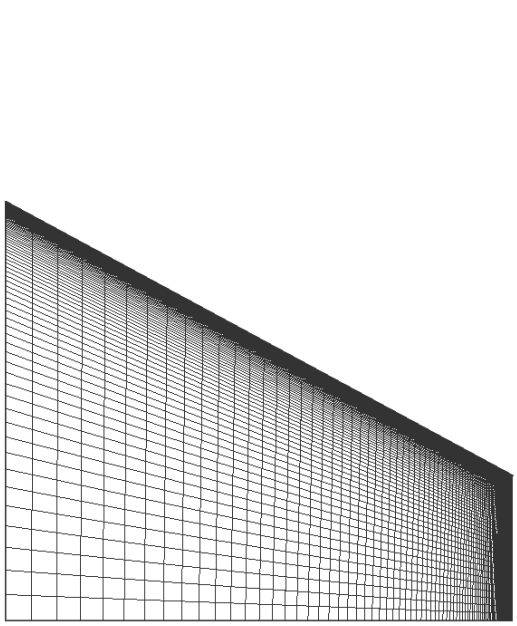

(a) Region-1(converging section)

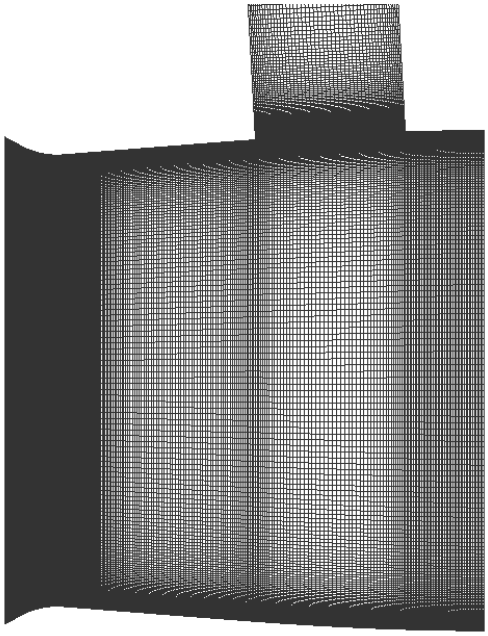

(b) Region-2(throat and diverging section)

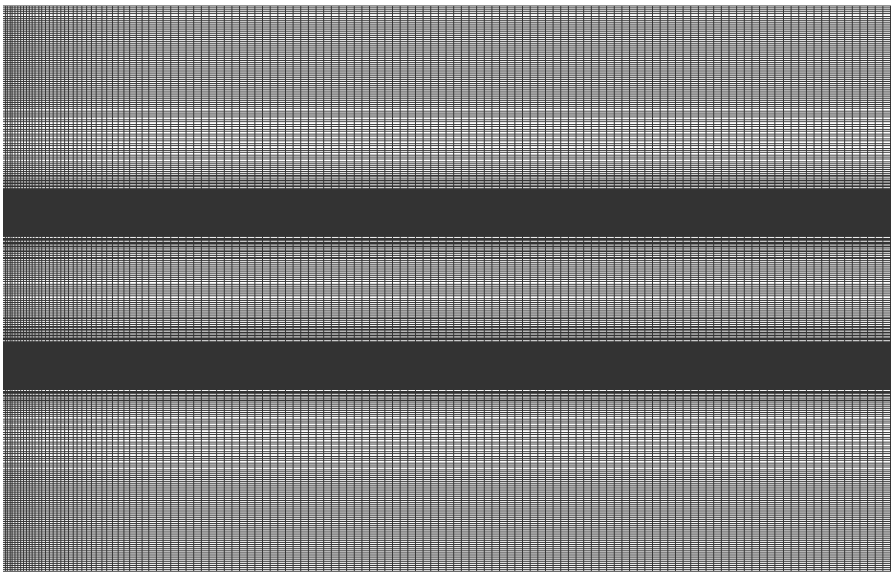

(c) Region-3(flow domain)

Figure 3.2.2: Zoomed mesh at various region for Mach 1.4

3.2.2. Mesh Independence Study

The nozzle has been designed for mach 1.4 and 1.6, hence, the mach number at exit of the nozzle is taken as a parameter for mesh independence study. As the number of elements significantly affect the value and the required development of flow, increasing the number of divisions with the same value in every edge, the number of elements and the average value of Mach number at exit has been tabulated in table 3.2.1 for Mach 1.4 and Mach 1.6.

Table 3.2.1: Mesh Independence Study

Mach Number	Number of Elements	Average Mach at exit of nozzle
1.4	4123	1.24789
	17804	1.38804
	39943	1.39026
	71653	1.39054
	112563	1.39061
	162673	1.39063
	221983	1.39067
1.6	1529	1.55514
	7380	1.56007
	29988	1.56203
	122463	1.56239
	277438	1.56245
	494913	1.56246
	774888	1.56247

For Mach 1.4, the value of mach number varied significantly from 4123 to 71653 number of elements. There is negligible variation in the exit mach number from 112563 number of elements. Similarly, for Mach 1.6, the value of mach number varied significantly from 1529 to 29988 number of elements. There is negligible variation in the exit mach number from 122463 number of elements. So, 112563 and 122463 number of elements has been chosen as the base number of element for conduction of simulations varying various parameters for Mach 1.4 and Mach 1.6 respectively.

The meshing pointwise file was exported in case file for the fluent 2D model.

3.2.3. Setup and Solution

Operating the fluent for the double precision calculation, the case file was read and different parameters were considered. For the high speed compressible flow, density based solver with steady-state conditions was chosen. The energy equations was enabled ON to capture the shock waves and to account for the temperature variations. A 2 equations turbulence model, standard $k-\varepsilon$ model was used to focus on fully turbulent flow. The material chosen for the flow was air with density defined by an ideal gas law, as it provides practical and accurate representation of air behaviour and accounts the variation of density with respect to change in pressure and temperature required for compressible flows. The Sutherland's law was considered for the viscosity to accurately model for the temperature dependency variation of dynamic viscosity in gases.

Implicit time stepping with AUSM scheme was taken to ensure the stability for high

speed flows and capture the shock waves and discontinuities. For capturing fine flow details and minimizing diffusion, second order discretization was chosen. THe boundary conditions used for simulation can be seen in figure 3.2.3 and figure 3.2.4 for without secondary inlet and with secondary inlet respectively. The setup and solutions parameters has been summarized in the table 3.2.2.

Table 3.2.2: Setup and solutions parameters

Outline	Parameters	Selected Options
General	Solver type Velocity Formulation Time 2D Space	Density-Based Absolute Steady Planar
Model	Energy Equation Turbulence Model	ON Standard $k-\varepsilon$ model
Materials(Fluid-Air)	Density Viscosity	Ideal Gas Sutherland (Three coefficient model)
Boundary Conditions	Operating Pressure Primary Inlet Pressure Secondary Inlet Pressure Outlet Pressure	0 Pascal 500000-700000 Pascal 100000-700000 Pascal 101325 Pascal
Solution	Methods Controls	Implicit time stepping, AUSM scheme, Second order discretization Courant Number = 0.5

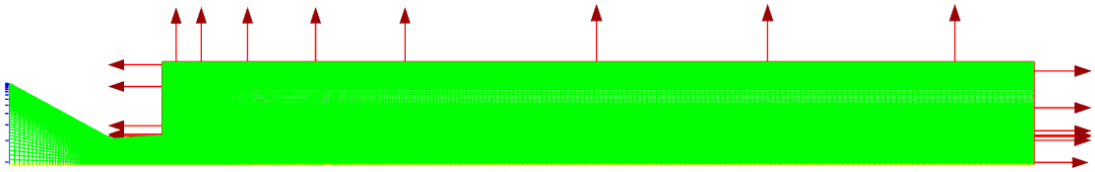

Figure 3.2.3: Boundary Conditions for Mach 1.4

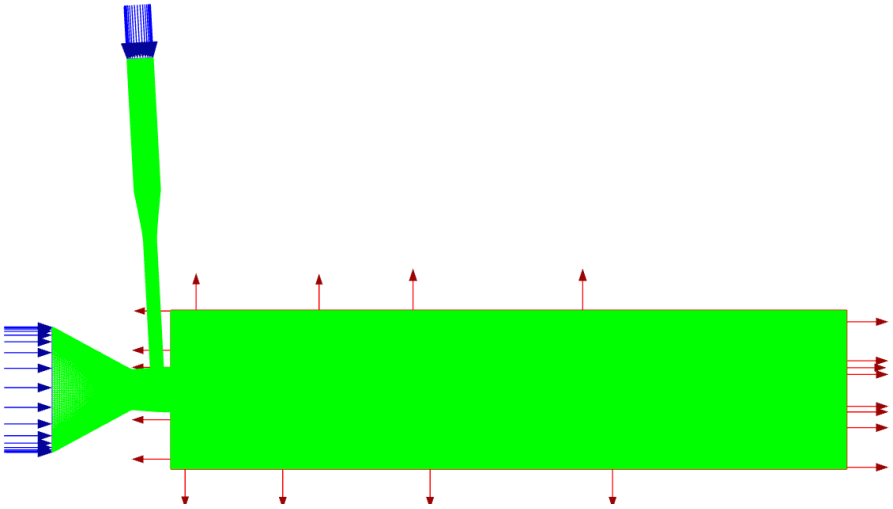

Figure 3.2.4: Boundary Conditions for Mach 1.4 with secondary

The standard initialization was performed by computing from the primary inlet. The calculation was run with solution steering for supersonic flow varying the courant number from 0.5 to 1 and updating the CFL. Reasonable convergence was obtained for all solutions with residuals 2 to 3 orders of magnitude.

3.3. Experimental Setup

3.3.1. CAD Model

The nozzle was modeled using SolidWorks based on the determined dimensions. The contour of the diverging section was generated using coordinates obtained from the Method of Characteristics (MOC) code and was extruded to a length of 4 mm.The converging section was designed as a cylindrical profile with an internal diameter of 33 mm and a wall thickness of 5 mm. The Loft feature was used to create a smooth transition between the converging and diverging sections.

The secondary inlet consisted of a tube with an outer diameter of 8 mm and an internal diameter of 4 mm, which converged to a 2 mm hole. It was positioned at 65% of the diverging section length and aligned tangent to the wall contour.

Additionally, a rectangular slot of 30 mm length was created in the diverging section to accommodate a glass sheet for flow visualization. The final 3D geometry was then prepared as shown in figure 3.3.1 and figure 3.3.2 without secondary and with secondary inlet respectively for printing.

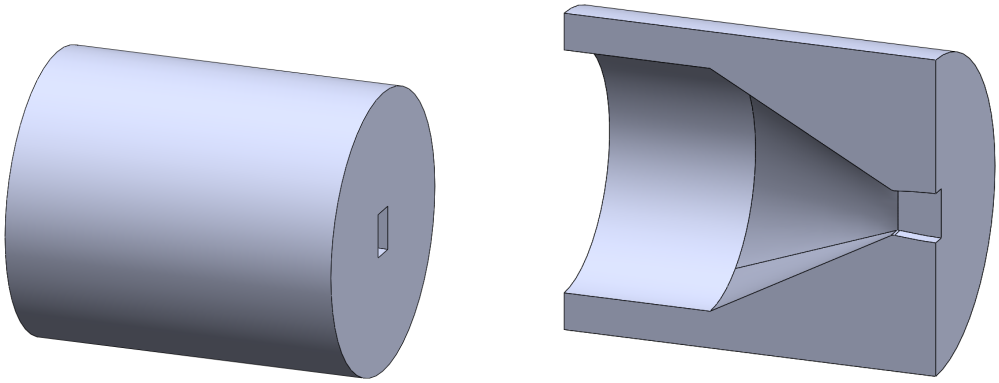

(a) 3D Geometry (b) Section view

Figure 3.3.1: 3D geometry for Mach 1.4

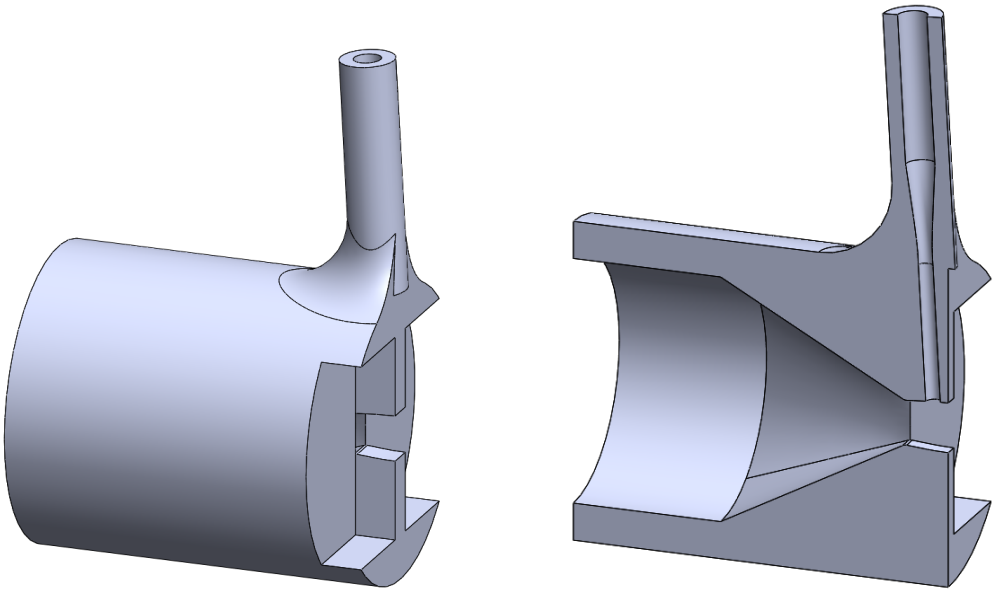

(a) 3D Geometry (b) Section view

Figure 3.3.2: 3D geometry with secondary inlet for Mach 1.4

3.3.2. Material selection and fabrication

After finalizing the model, the design was exported as an STL file and imported into the slicing software for the 3D printer available at the Department of Mechanical and Aerospace Engineering (DMAE). PolyLactic Acid (PLA) was selected as the printing material due to its ease of use, availability, good resolution, and minimal warping. 3D printed nozzles for various Mach number, with and without secondary inlet is shown in figure 3.3.3. After printing, a 1.5 mm thick glass sheet was cut to match the dimensions of the designated slot in the diverging section and was fixed in place using a high-strength adhesive.

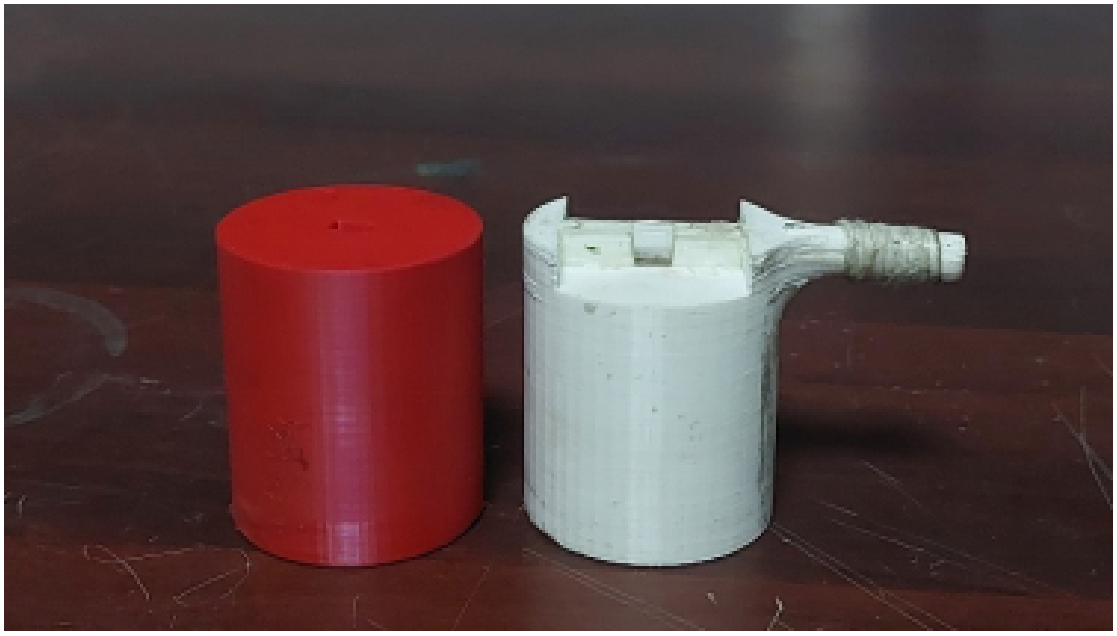

(a) Mach 1.4

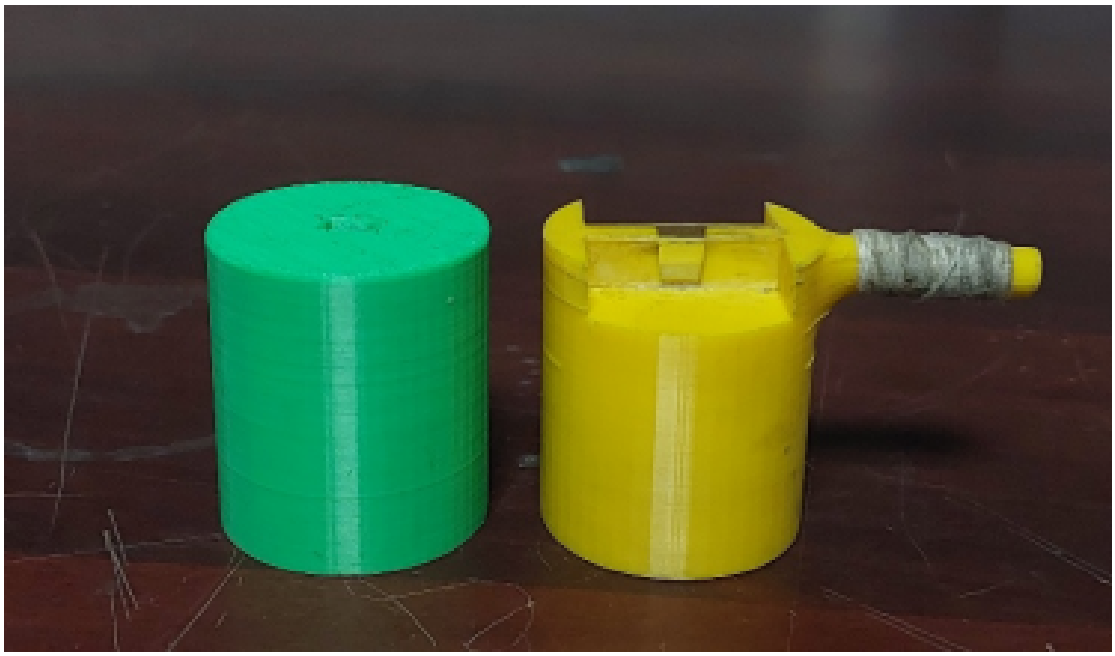

(b) Mach 1.6

Figure 3.3.3: 3D printed nozzle without and with secondary inlet

3.3.3. Thrust Vectoring Setup

The experimental setup was used to deliver pressurized air into the nozzle, originally developed by [24], was modified to incorporate secondary flow injection for thrust vectoring. The setup utilizes two air compressors to supply high-pressure air to the nozzle's primary and secondary inlets. A 2 HP, 70 L air compressor was used to supply the primary air to the nozzle, while a 1 HP, 20 L compressor was used to supply the secondary

air. Secondary air injection plays a crucial role in adjustment of the thrust vector, influencing the direction and control of the jet flow. Both compressors operate safely at a maximum pressure of 8 bars, ensuring a high-pressure airflow supply.

At the outlets of both compressors, 0.25-inch ball valves were installed to deliver air through polyurethane (PU) pipes of 8 mm internal diameter. To provide precise actuation and timing control, solenoid valves were installed, which operated on a 12 V DC, provided by an AC to DC power supply unit. A 3D printed switch box with three toggle switches was installed to control the flow as required.

For thrust vectoring with time delay, the middle switch should be turned ON first, followed by the turning ON of the left and right switch with required time delay. Similarly, for simultaneous operation or vectoring without any delay, the left and right switch should be turned ON first, followed by turning ON of the middle switch. The schematic drawing and flow control circuit for the setup can be seen in figure 3.3.4 and figure 3.3.5 respectively. This configuration ensures controlled activation of the compressed air supply.

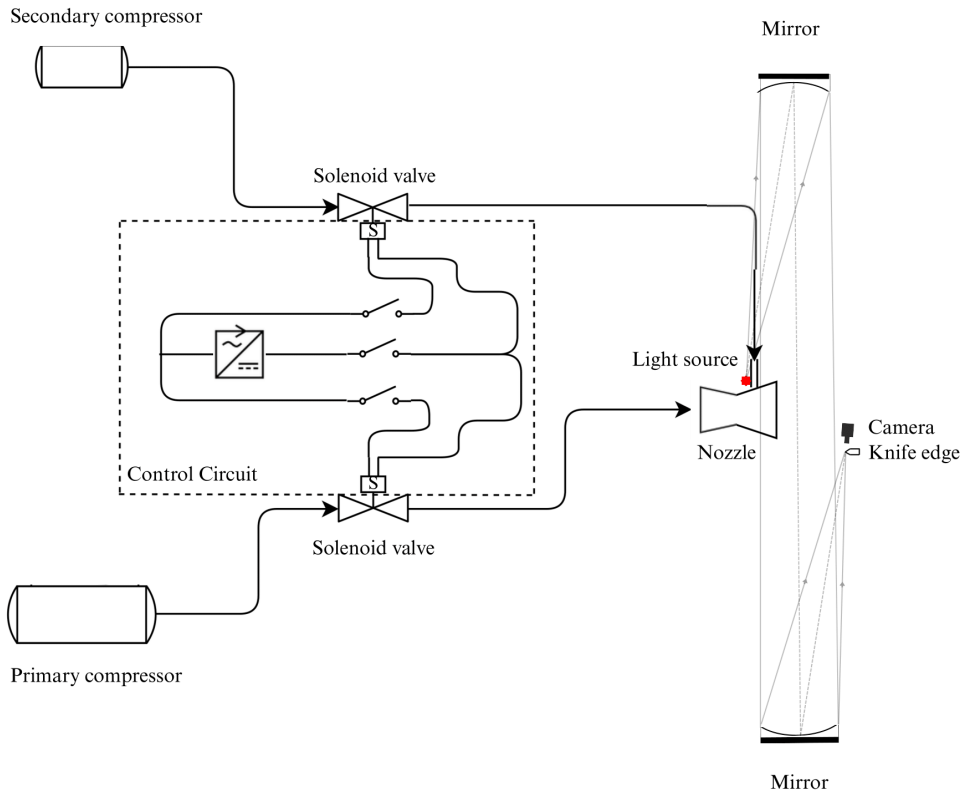

Figure 3.3.4: Schematic Drawing of the Experimental Setup

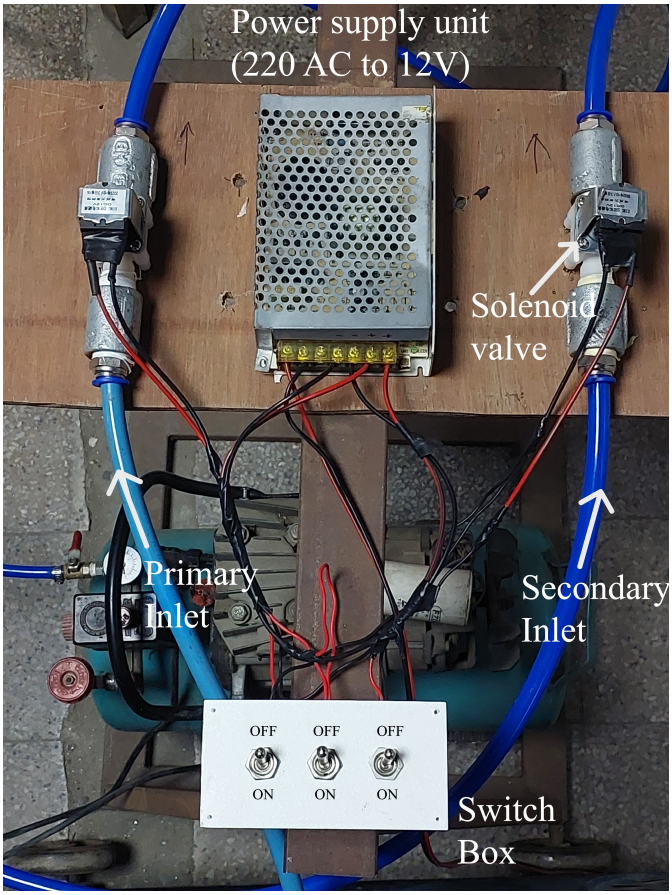

Figure 3.3.5: Flow Control Circuit

The complete setup consisted of two compressors, ball valves, PU pipes, solenoid valves, control circuit, a test stand, and clamps to deliver compressed air to the inlet of nozzle.

3.3.4. Flow Visualization

3.3.4.1. Z-type Schlieren Method

The Z-type Schlieren method was selected to visualize and study the exhaust flow from the nozzle due to its high sensitivity to small density gradients and its ability to capture flow phenomena in high-speed flows. The setup, developed by [1] at DMAE, as shown in figure 3.3.6, was utilized for this purpose. The setup consists of two parabolic mirrors, each with a focal length of 400 mm and a diameter of 76 mm. These mirrors are used to direct a beam of light through the test section, where the nozzle exhaust flow is located. A white LED light source, powered by a 9V battery, is used with a 280-ohm resistor connected in series to prevent potential damage to the light source.

The light beam is reflected from the first parabolic mirror to form a parallel beam that

passes through the nozzle exhaust, which is located at the center and at a height of 16 cm from the platform. The light is then passed to the second mirror, which focuses the image onto a knife-edge. The knife-edge is positioned at the focal distance of the second mirror and serves to partially obstruct the refracted light, thus controlling the sensitivity to density gradients within the flow.

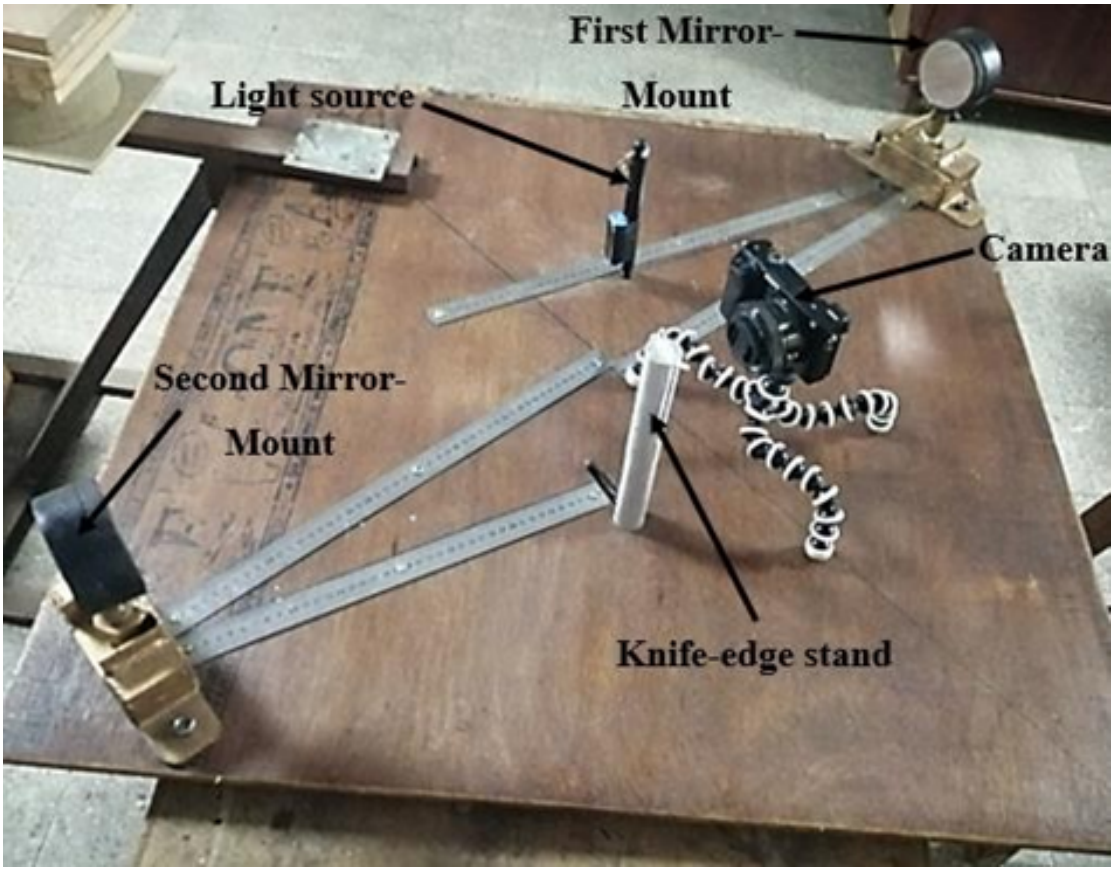

Figure 3.3.6: Z-Type Schlieren Setup[1]

The resulting Schlieren image was recorded using a Sony ZV-E10 mirrorless camera mounted on a Gorilla tripod stand. The camera settings were manually configured with a shutter speed of 1/1600 seconds, an aperture of f/5.6, ISO 160, and an exposure of -2. These settings were selected based on the image clarity and contrast required for capturing the shock patterns of the under-expanded exhaust jet. The full experimental setup that was used for the experiments is shown in figure 3.3.9.

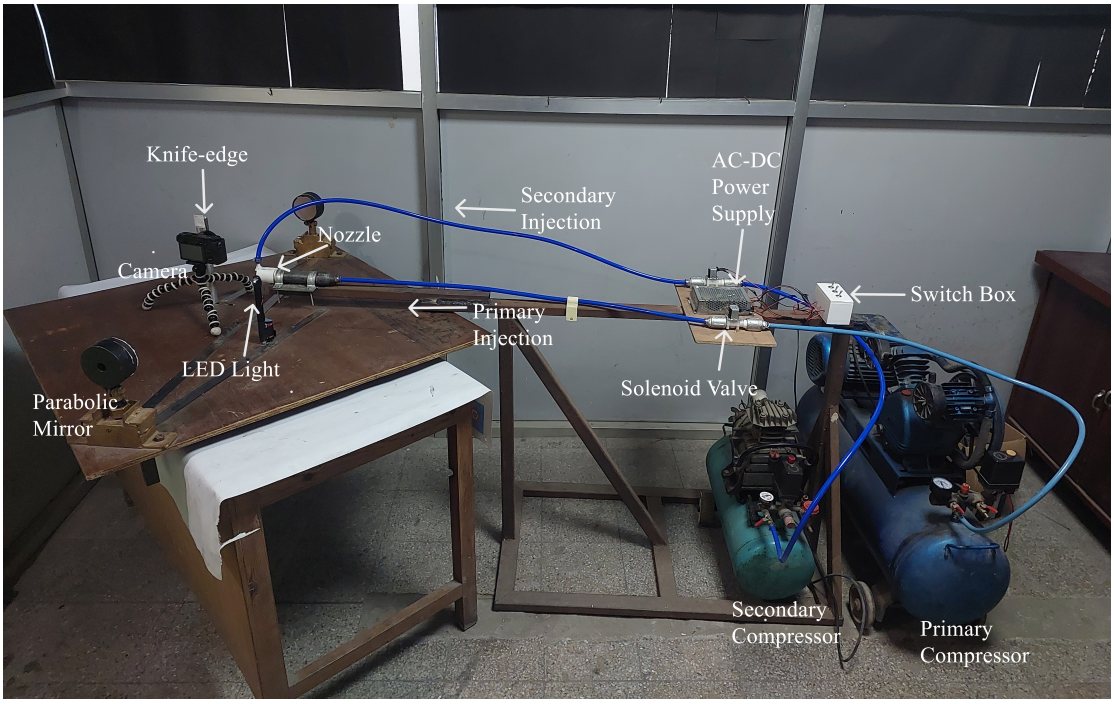

Figure 3.3.7: Full Experimental Setup

3.4. Post Processing

3.4.1. Simulation Post Processing

3.4.1.1. Data Calculation

After the completion of simulation, a line was created at the exit of the nozzle for each nozzle of different Mach number. Then, the data of each point of a line for density, u velocity and v velocity were exported in excel. Using these datas, the mass flux was calculated at the exit of the nozzle.

$$Massflux = \dot{m} = A_e \times \rho_e \times v_e$$

Mass flux was calculated for nozzle without and with secondary inlet for each data points and average was calculated and taken for finding the deflection angle. The deflection angle was calulated as:

$$\theta_{\text{without secondary}} = \tan^{-1}\left(\frac{\rho \times v}{\rho \times u}\right)$$

$$\theta_{\text{with secondary}} = \tan^{-1}\left(\frac{\rho \times v}{\rho \times u}\right)$$

$$\theta_{\text{deflection}} = \theta_{\text{with secondary}} - \theta_{\text{without secondary}}$$

3.4.1.2. Using ImageJ

The density contours were imported to ImageJ for calculation of deflection angle and distance measurement. In ImageJ, scale was set according to the exit height of nozzle, which is the known distance. At first, a line coincident to the nozzle exit was drawn, then a perpendicular line was drawn from the center line of nozzle. This perpendicular line was taken as the reference line for measuring angle. Three point angle tool was used which required two lines to be drawn. So, a horizontal line was drawn coincident to the reference line and a straight line was drawn joining the intersection points of the shock diamonds, which gave the values of deflection angle as shown in figure 3.4.1.

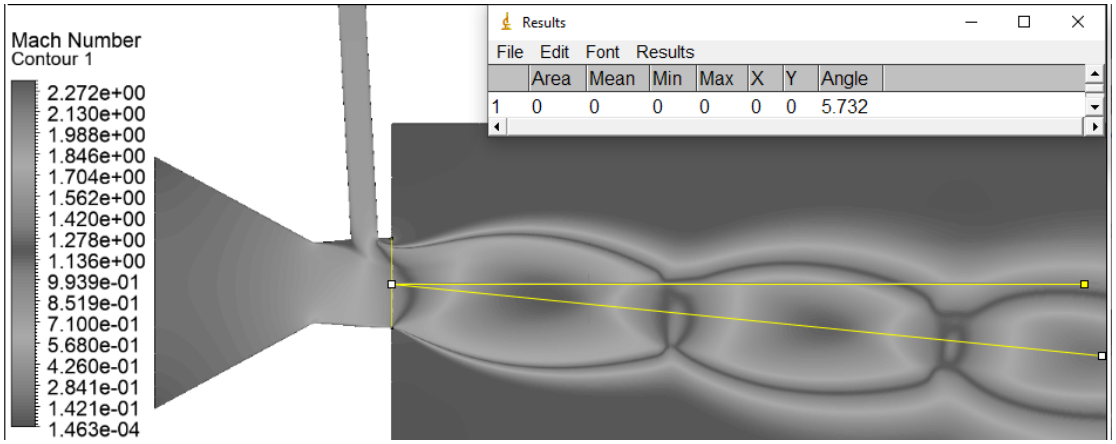

Figure 3.4.1: Angle Measurement using density contour for Mach 1.4 at NPR 5 and Secondary Pressure 5 bar

Distance between the nozzle exit and first stronger shock diamond formed was also measured using imageJ. For this, a straight parallel line was drawn at the nozzle exit and also a line perpendicular to the shock diamond was drawn. The length between these two lines were measured which provided the value of required distance as shown in figure 3.4.2.

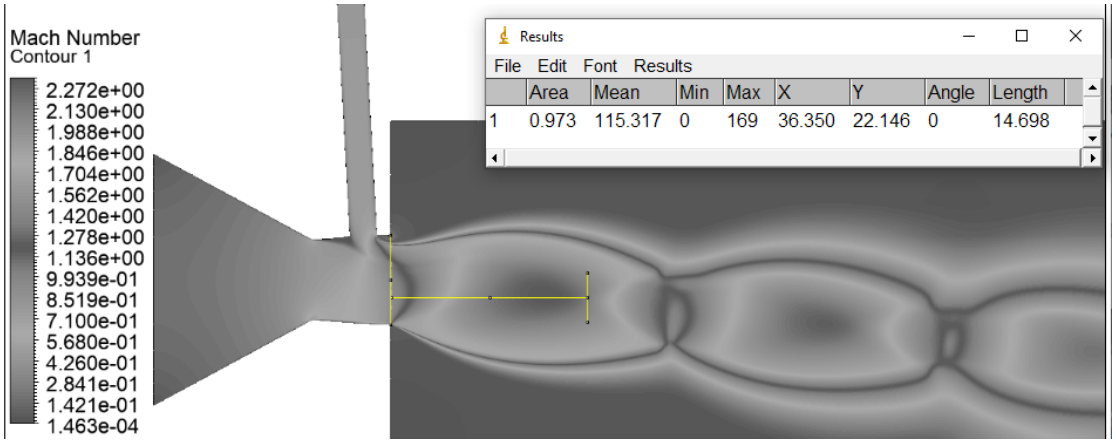

Figure 3.4.2: Distance Measurement using density contour for Mach 1.4 at NPR 5 and Secondary Pressure 5 bar

3.4.2. Experimental Post Processing

For post processing, images were firstly extracted from videos and then they were imported into image manipulation software, GIMP, where brightness, contrast and exposure of the image were adjusted accordingly to clearly visualize the shock diamonds. Once the images were ready, they were imported to ImageJ for calculation of deflection angle. Deflection angles and distance between the nozzle exit and first stronger shock diamonds were measured implementing the similar method used for density contours as shown in figure 3.4.3 and figure 3.4.4.

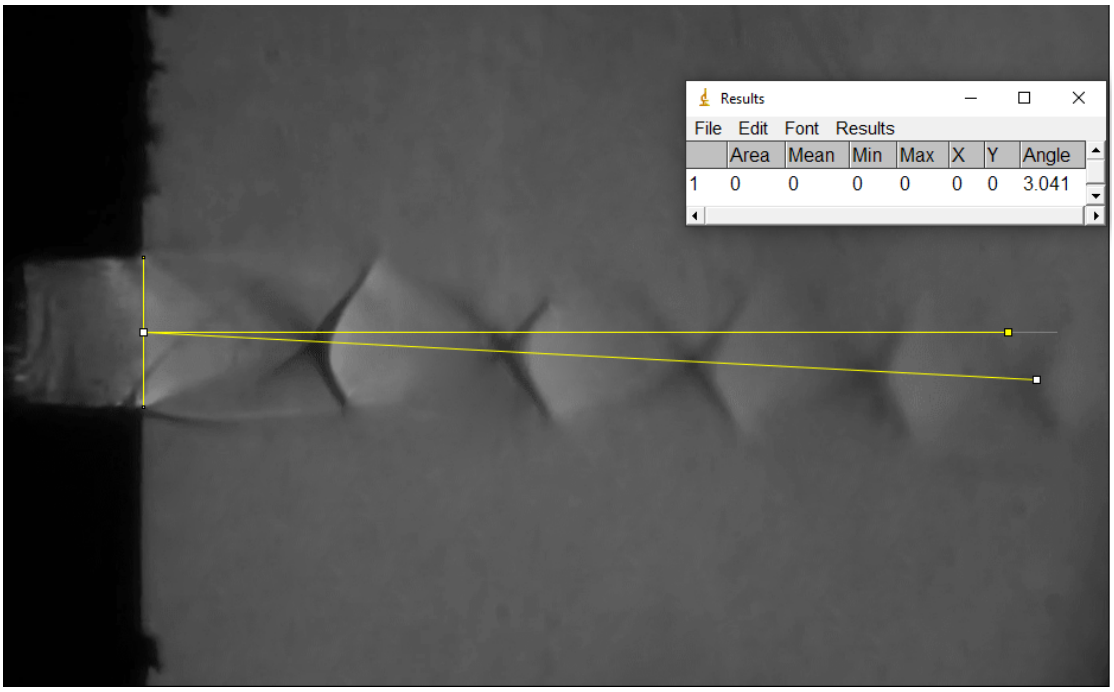

Figure 3.4.3: Angle Measurement of Experimental Picture obtained for Mach 1.4 NPR 6 Secondary Pressure 2 bar

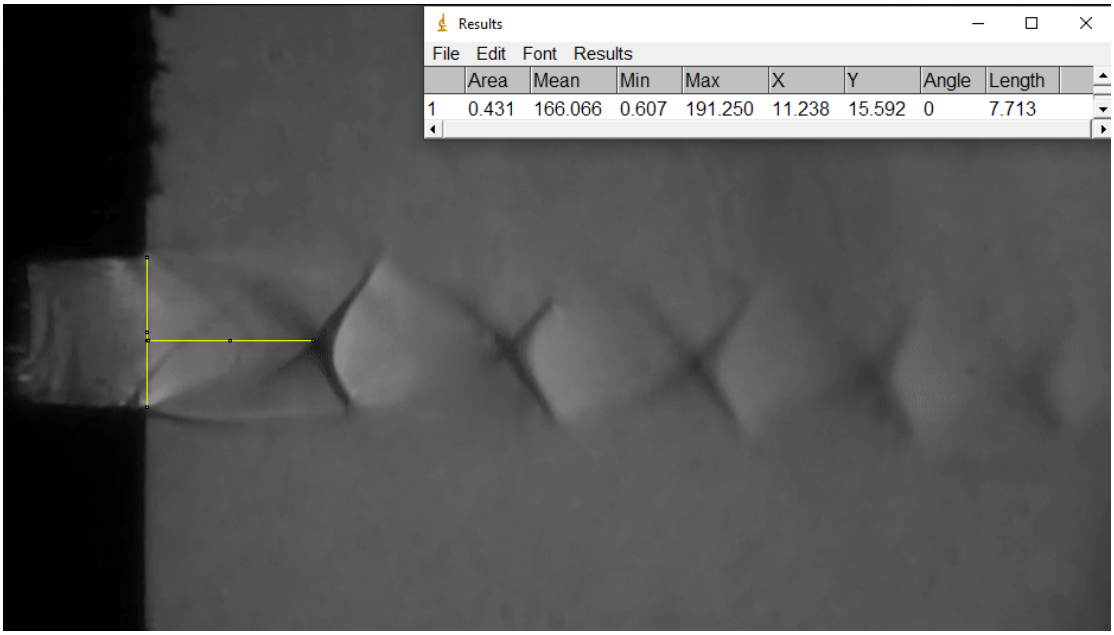

Figure 3.4.4: Distance Measurement of Experimental Picture obtained for Mach 1.4 NPR 6 Secondary Pressure 2 bar

CHAPTER 4:
RESULT AND DISCUSSIONS

4.1. Output

4.1.1. Numerical Simulation Results

The numerical simulation was conducted for half-domain and reflected about the symmetry for the full flow simulation result of the velocity contour for nozzle without secondary inlet. The simulation for nozzle without secondary inlet was done for inlet pressure of 5 bar, 6 bar and 7 bar. The inlet pressure for perfectly expanded nozzle for Mach 1.4 is 3.22 bar and for Mach 1.6 is 4.31 bar. Hence, the inlet pressure has been chosen for the under expanded condition of the nozzle for both Mach number.

For the simulation of nozzle with secondary inlet, the full domain mesh was created and simulation result for velocity contours were obtained. Secondary pressure were varied from 1 bar to 5 bar for NPR 5, 1 bar to 6 bar for NPR 6 and 1 bar to 7 bar for NPR 7. Secondary pressures were chosen in such a manner so that the SPR doesn't exceed the value of 1 for each NPR.

From the velocity contour without secondary inlet, the distinct Mach diamonds can be seen with increment in its distance from the exit of the nozzle and no deflection can be seen in the flow as expected. Observing the velocity contour of NPR 5,6 and 7 for secondary pressure of 1 bar, the deflection of the flow is slightly negative. Also, there is suction of primary flow into the secondary inlet due to large pressure difference between the flow. For secondary pressure of 2 bar, there is minimum or no deflection. Increasing the secondary pressure has the positive influence on the deflection angle. The deflection angle was observed to be maximum when secondary inlet pressure was kept equal to primary inlet pressure i.e. at SPR = 1. The similar trends can be seen for both Mach 1.4 and Mach 1.6.

The velocity contours for Mach 1.4 can be seen in Figure 4.1.1 without secondary inlet and Figure 4.1.2, Figure 4.1.3 and Figure 4.1.4 for NPR 5, 6 and 7 respectively, with varying secondary pressure from 1 bar to 7 bar.

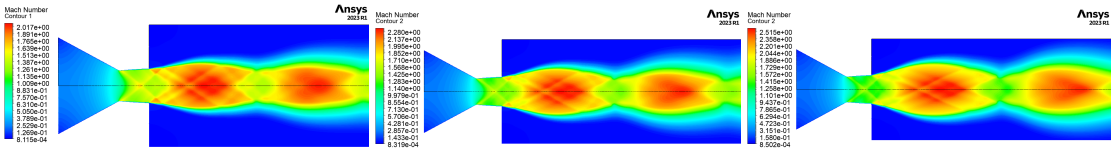

(a) 5 bar (b) 6 bar (c) 7 bar

Figure 4.1.1: Velocity Contours without secondary inlet for Mach 1.4

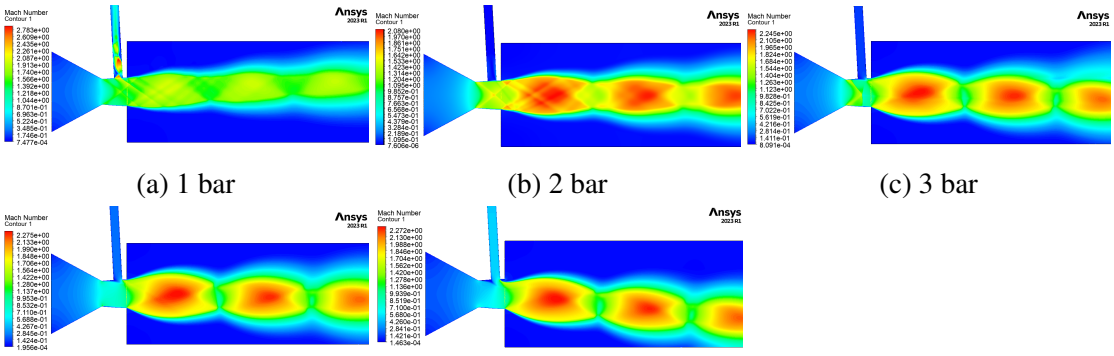

(a) 1 bar (b) 2 bar (c) 3 bar

(d) 4 bar (e) 5 bar

Figure 4.1.2: Velocity Contours at NPR 5 for various Secondary Pressure for Mach 1.4

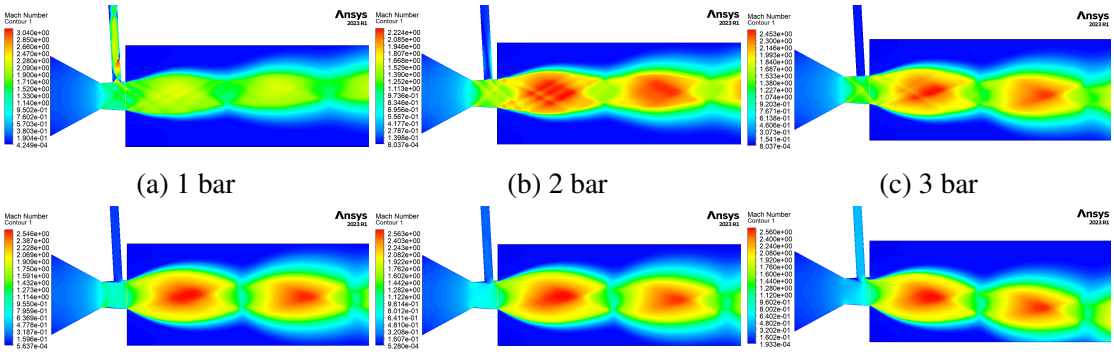

(a) 1 bar (b) 2 bar (c) 3 bar

(d) 4 bar (e) 5 bar (f) 6 bar

Figure 4.1.3: Velocity Contours at NPR 6 for various Secondary Pressure for Mach 1.4

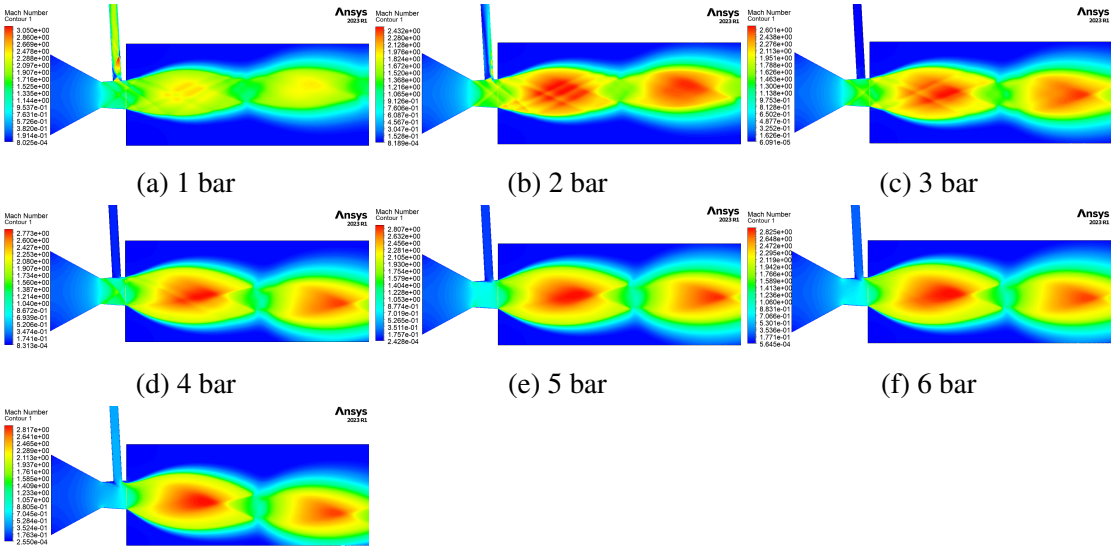

(a) 1 bar (b) 2 bar (c) 3 bar

(d) 4 bar (e) 5 bar (f) 6 bar

(g) 7 bar

Figure 4.1.4: Velocity Contours at NPR 7 for various Secondary Pressure for Mach 1.4

The velocity contours for Mach 1.6 can be seen in Figure 4.1.5 for without secondary inlet and Figure 4.1.6, Figure 4.1.7 and Figure 4.1.8 for NPR 5, 6 and 7 respectively, with varying secondary pressure from 1 bar to 7 bar.

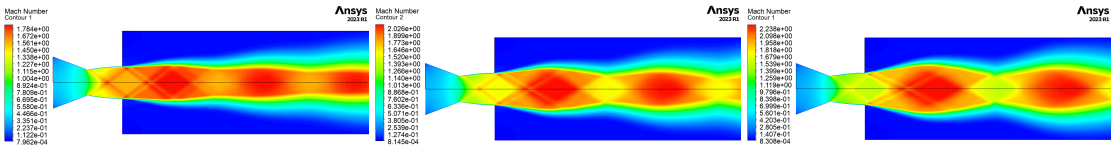

(a) 5 bar (b) 6 bar (c) 7 bar

Figure 4.1.5: Velocity Contours without secondary inlet for Mach 1.6

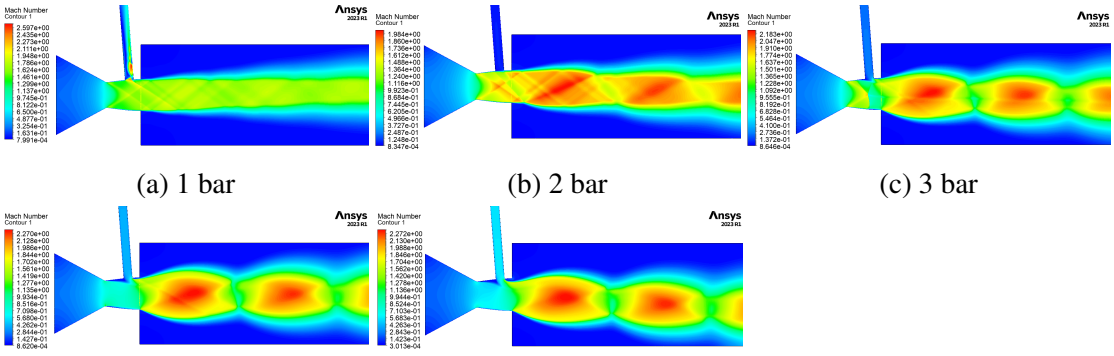

(a) 1 bar (b) 2 bar (c) 3 bar

(d) 4 bar (e) 5 bar

Figure 4.1.6: Velocity Contours at NPR 5 for various Secondary Pressure for Mach 1.6

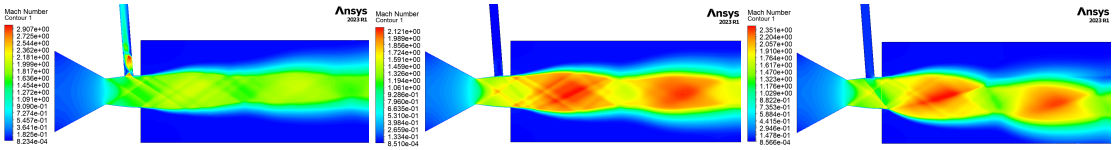

(a) 1 bar (b) 2 bar (c) 3 bar

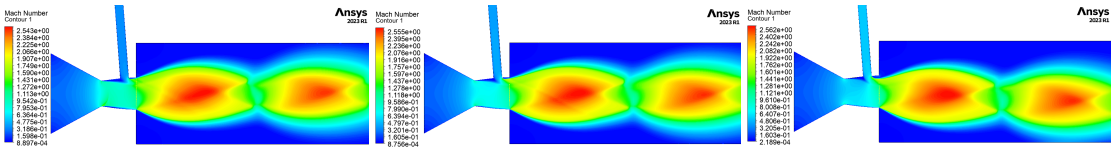

(d) 4 bar (e) 5 bar (f) 6 bar

Figure 4.1.7: Velocity Contours at NPR 6 for various Secondary Pressure for Mach 1.6

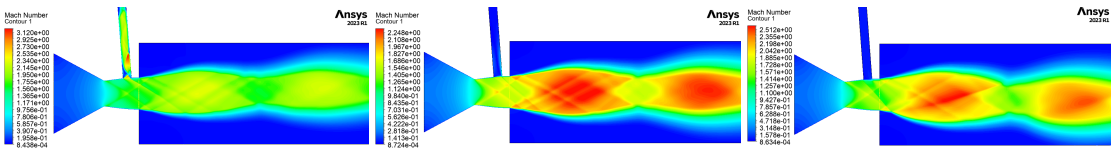

(a) 1 bar (b) 2 bar (c) 3 bar

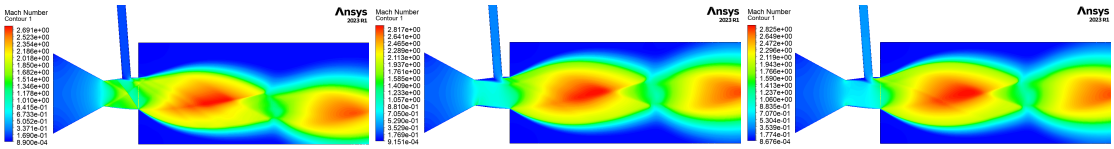

(d) 4 bar (e) 5 bar (f) 6 bar

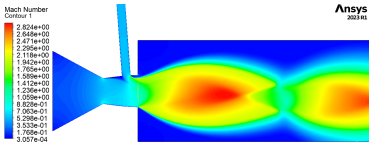

(g) 7 bar

Figure 4.1.8: Velocity Contours at NPR 7 for various Secondary Pressure for Mach 1.6

4.1.2. Experimental Results

Firstly, the experiment for nozzle without secondary inlet was done for primary inlet pressure of 5 bar, 6 bar and 7 bar. Secondary pressure were varied from 1 bar to 5 bar for NPR 5, 1 bar to 6 bar for NPR 6 and 1 bar to 7 bar for NPR 7. For each values of secondary inlet pressure and NPR, experiment was conducted thrice ultimately acheiving average deflection. Deflection obtained for nozzle without secondary inlet was taken as initial deflection which was utilized to calculate the net deflection.

For nozzle without secondary inlet, no significant deflection was achieved. Experimental results showed greater deflection angle at lower NPR, higher SPR and higher Mach number. For every NPR values, there was rise in deflection angle with the increase in secondary pressure.

The schlieren images for Mach 1.4 can be seen in Figure 4.1.9 for without secondary inlet and Figure 4.1.10, Figure 4.1.11 and Figure 4.1.12 for NPR 5, 6 and 7 respectively, with varying secondary pressure from 1 bar to 7 bar.

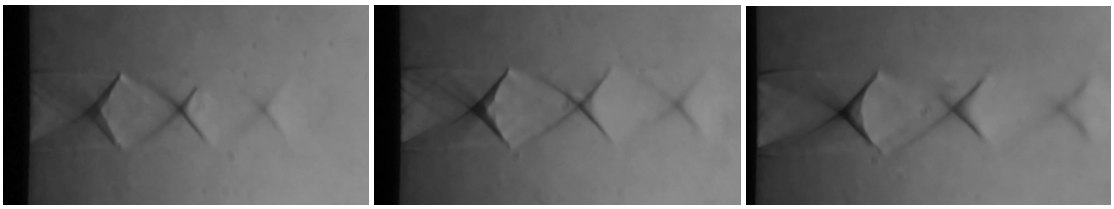

(a) 5 bar (b) 6 bar (c) 7 bar

Figure 4.1.9: Schlieren Images without secondary inlet for Mach 1.4

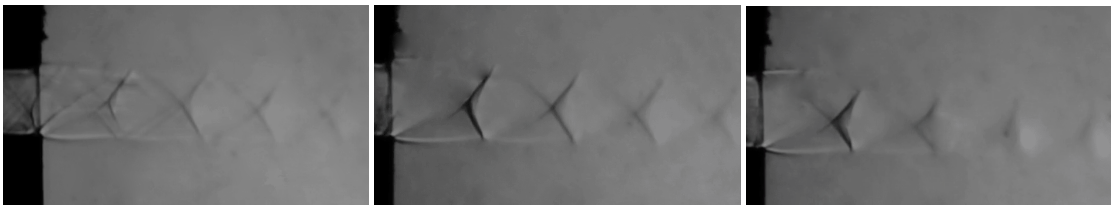

(a) 1 bar (b) 2 bar (c) 3 bar

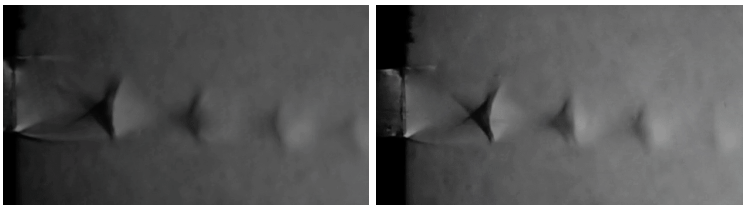

(d) 4 bar (e) 5 bar

Figure 4.1.10: Schlieren Images at NPR 5 for various Secondary Pressure for Mach 1.4

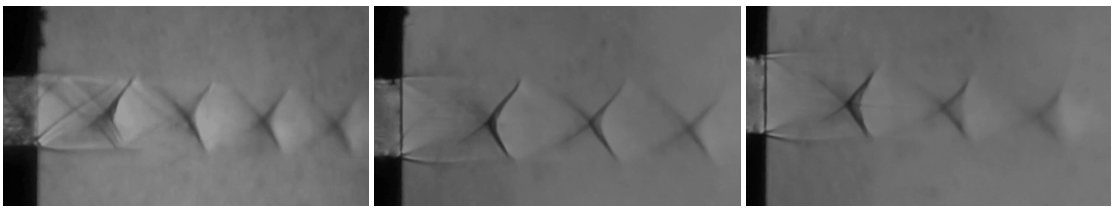

(a) 1 bar (b) 2 bar (c) 3 bar

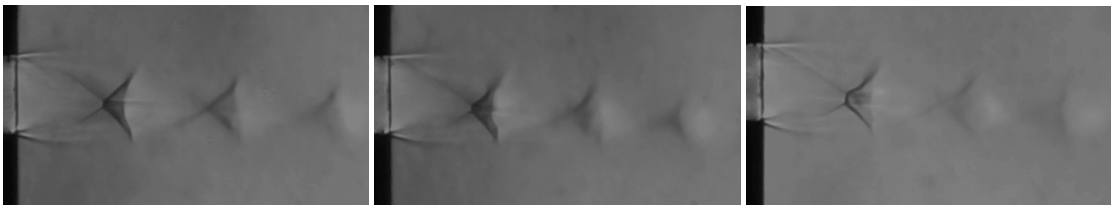

(d) 4 bar (e) 5 bar (f) 6 bar

Figure 4.1.11: Schlieren Images at NPR 6 for various Secondary Pressure for Mach 1.4

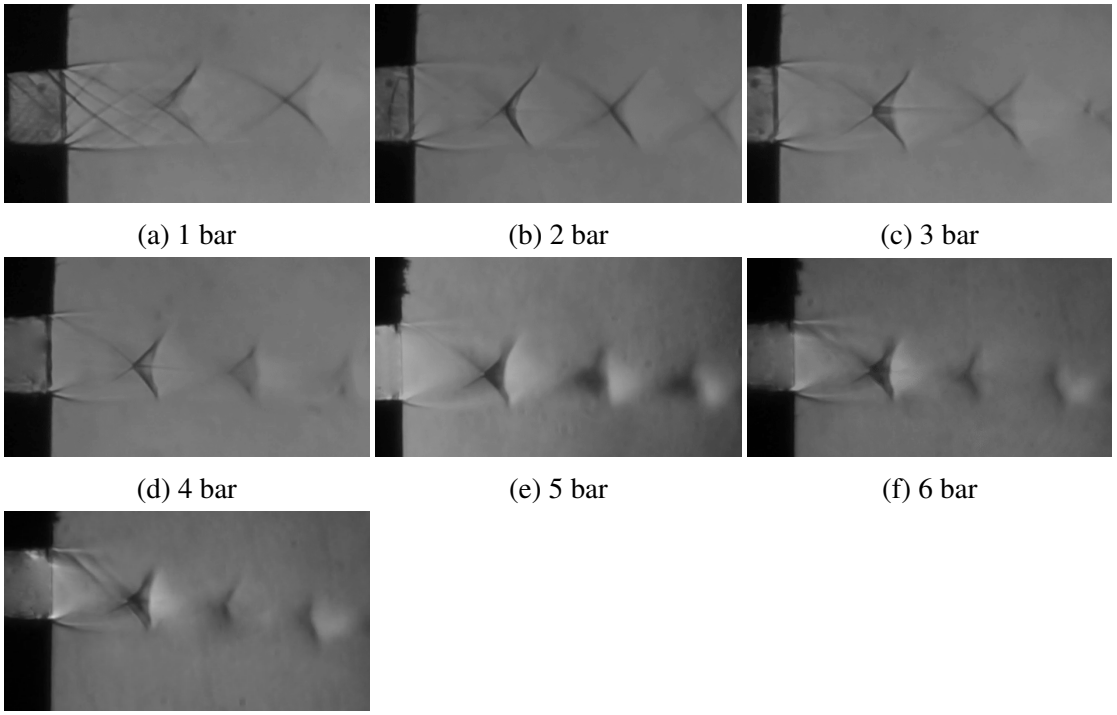

(a) 1 bar (b) 2 bar (c) 3 bar

(d) 4 bar (e) 5 bar (f) 6 bar

(g) 7 bar

Figure 4.1.12: Schlieren Images at NPR 7 for various Secondary Pressure for Mach 1.4

The schlieren images for Mach 1.6 can be seen in Figure 4.1.13 for without secondary inlet and Figure 4.1.14, Figure 4.1.15 and Figure 4.1.16 for NPR 5, 6 and 7 respectively.

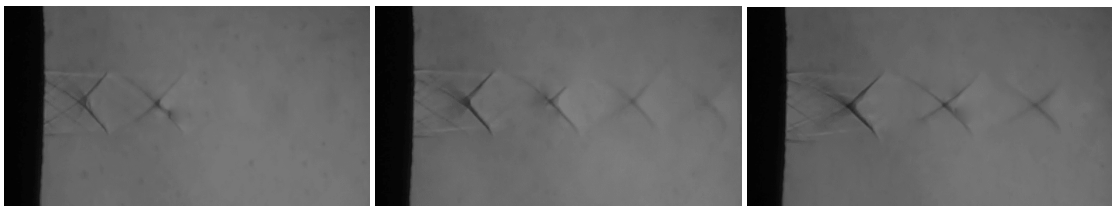

(a) 5 bar (b) 6 bar (c) 7 bar

Figure 4.1.13: Schlieren Images without secondary inlet for Mach 1.6

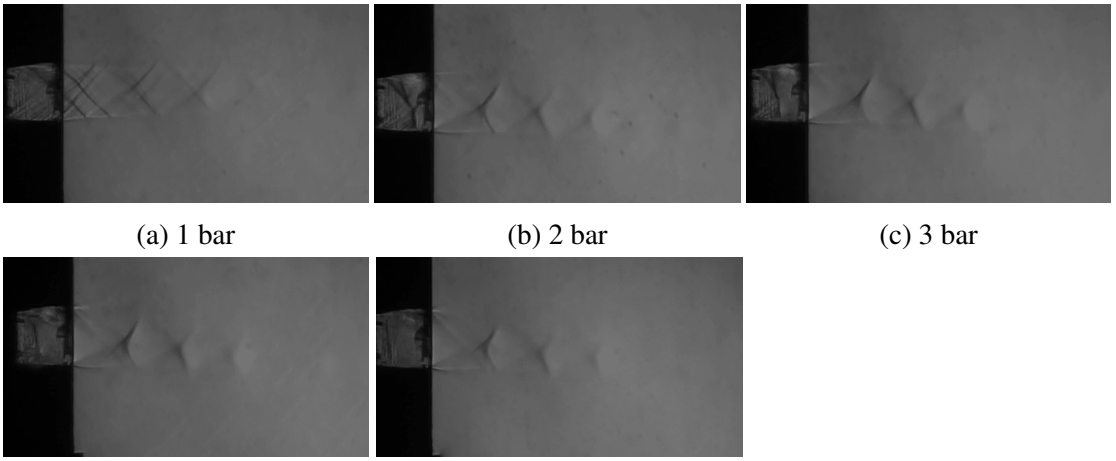

(a) 1 bar (b) 2 bar (c) 3 bar

(d) 4 bar (e) 5 bar

Figure 4.1.14: Schlieren Images at NPR 5 for various Secondary Pressure for Mach 1.6

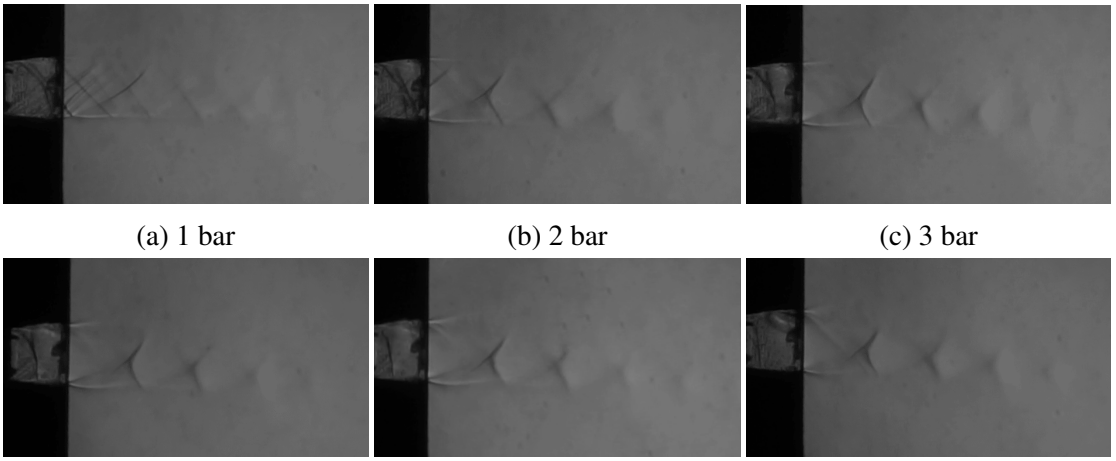

(a) 1 bar (b) 2 bar (c) 3 bar

(d) 4 bar (e) 5 bar (f) 6 bar

Figure 4.1.15: Schlieren Images at NPR 6 for various Secondary Pressure for Mach 1.6

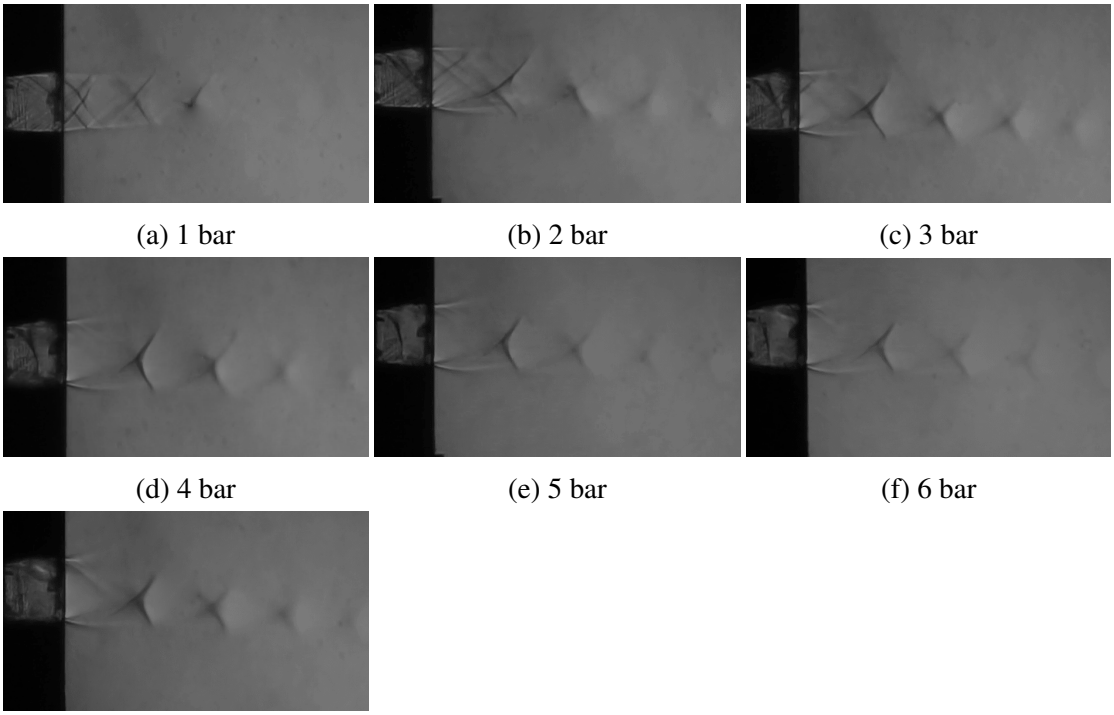

(a) 1 bar (b) 2 bar (c) 3 bar

(d) 4 bar (e) 5 bar (f) 6 bar

(g) 7 bar

Figure 4.1.16: Schlieren Images at NPR 7 for various Secondary Pressure for Mach 1.6

4.2. Result Analysis

4.2.1. Data Collection

The experimental and numerical simulations were conducted for Mach 1.4 and Mach 1.6 nozzles at NPR values of 5, 6, and 7, with secondary pressures ranging from 1 bar to the respective primary pressure. Pressure was simultaneously injected into the primary inlet and secondary inlet of the nozzle from the primary and secondary compressor respectively with the help of solenoid valve. The results obtained are then analyzed in terms of experimental deflection angles, deflection angles obtained from CFD image processing using ImageJ, and numerical simulation data. Following observations were made:

4.2.1.1. Deflection Angle Trends for Mach 1.4 Nozzle

For NPR 5, as the SPR increased from 0.2 to 1, the experimental deflection angle progressively increased from 1.717° to 4.454°. A similar increasing trend was observed in the numerical simulation data, reaching a maximum deflection of 6.185°. The CFD image-based deflection values followed similar increasing trend,with some negative values for lower SPRs.

For NPR 6, the experimental deflection varied between 1.116° and 4.416°, while the numerical results showed a peak deflection of 5.397°. The deflection angles derived from ImageJ were lower, with some negative values at lower SPRs.

At NPR 7, the experimental deflection ranged from -0.803° to 6.140. The numerical simulation values followed a similar increasing trend but the values differed significantly by 2 or 3 degrees at larger SPR values.ImageJ-derived values varied significantly at lower SPRs, with negative values observed for SPRs below 0.429.

4.2.1.2. Deflection Angle Trends for Mach 1.6 Nozzle

For NPR 5, the experimental deflection increased from 1.131° at SPR 0.2 to 7.092° at SPR 1. Numerical simulation data showed a similar trend, with the highest deflection reaching just 4.275. The ImageJ-based deflection values fluctuated, with some negative results for lower SPRs.

For NPR 6, the experimental deflection started at 2.001° and increased to 7.449° as SPR increased from 0.167 to 1 degree. The simulation data exhibited a peak deflection of 2.811°, whereas ImageJ-derived values followed a non-linear pattern with variations.

At NPR 7, experimental deflection varied from -1.161° to 6.398°, with numerical values reaching a maximum of 2.902°. The ImageJ-based deflection showed fluctuated deviations, with lower SPRs producing negative deflection angles.

4.2.1.3. Effect of Increasing NPR and SPR on Deflection

At a fixed NPR, increasing SPR led to a higher deflection angle, confirming the expected influence of secondary injection on deflection angle.

For a given SPR, there was rise and fall of deflection angle with the increment in NPR. The deflections remain relatively small across all NPRs, especially at NPR 5. With the increment in secondary inlet pressures, deflection angles were rising for high NPRs, particularly at NPR 7, where maximum defelctions were observed. This indicates that at higher NPRs, primary flow is more dominant and a stronger secondary flow is required to achieve significant vectoring. Experimental data showed a maximum deflection of 7.449 degrees obtained at NPR 6 and SPR 1 at Mach 1.6 whereas minimum deflection of -0.803 degrees was obtained at NPR 7 and SPR 1 at Mach 1.4.

The Mach 1.6 nozzle exhibited higher deflection values compared to Mach 1.4 for the same NPR and SPR conditions.

The data that were calculated using experimental setup, schlieren based measurement and simulation data are gathered in the table 4.2.1.

Table 4.2.1: Deflection Angle

Mach	NPR	Secondary Pressure	SPR	Deflection Angle		
				Experimental	Simulation (ImageJ)	Simulation Data
1.4	5	1	0.2	1.717	-3.643	-1.668
		2	0.4	2.381	-1.052	1.718
		3	0.6	2.809	0.830	1.837
		4	0.8	3.893	0.845	2.248
		5	1	4.454	6.580	6.185
	6	1	0.167	1.116	-3.670	-1.503
		2	0.333	1.764	-2.230	-0.638
		3	0.5	3.025	1.050	1.713
		4	0.667	3.190	0.060	1.848
		5	0.833	3.596	3.658	2.088
		6	1	4.416	6.160	5.397
	7	1	0.143	-0.803	-3.720	-0.889
		2	0.286	2.364	-3.030	1.534
		3	0.429	2.724	-0.606	1.759
		4	0.571	3.807	3.180	2.817
		5	0.714	4.099	0.040	1.418
		6	0.857	5.186	1.270	1.863
		7	1	6.140	5.700	4.979
1.6	5	1	0.2	1.131	-2.014	-2.499
		2	0.4	4.531	0.946	2.891
		3	0.6	5.027	0.876	3.431
		4	0.8	6.016	-0.138	4.190
		5	1	7.092	3.666	4.275
	6	1	0.167	2.001	-2.284	1.424
		2	0.333	5.866	-0.304	1.540
		3	0.5	5.874	3.406	2.342
		4	0.667	6.568	1.015	1.125
		5	0.833	6.721	-0.044	2.395
		6	1	7.449	3.016	2.811
	7	1	0.143	-1.161	-2.308	1.374
		2	0.286	5.043	-1.061	1.525
		3	0.429	5.076	1.472	2.259
		4	0.571	5.154	6.002	4.326
		5	0.714	5.392	-0.988	1.454
		6	0.857	5.685	-0.177	1.810
		7	1	6.398	2.732	2.902

4.2.2. Evaluation of Plot

Figure 4.2.1 (a) and Figure 4.2.2 (a) shows the experimental data , where the deflection angle is increasing gradually with the increase in secondary pressure for all NPR values. This could be due to the greater influence of secondary flow injection on deflection at a constant NPR. A slightly greater deflection angle is observed at NPR 5 followed by NPR 7 and 6 for Mach 1.4 whereas, high deflection is observed at NPR 5 followed by NPR 6 and 7 for Mach 1.6. The experimental results for Mach 1.6 shows higher deflection angles than Mach 1.4, with saturation in deflection angle beyond certain SPR values, especially for NPR 6 and 7. This indicates that lower NPR and higher Mach could be more effective for thrust vectoring.

Figure 4.2.1 (b) and Figure 4.2.2 (b) represents the simulation data obtained from CFD post processing while Figure 4.2.1 (c) and Figure 4.2.2 (c) represents imageJ based measurements. Both showed a similar increasing trend of deflection angle with the increase in secondary pressure, but at higher values, trend becomes non linear. Simulation results showed variations from experimental data, especially for NPR 7, where peak is observed. Mach 1.6 introduced more variations and inconsistencies in simulation results.

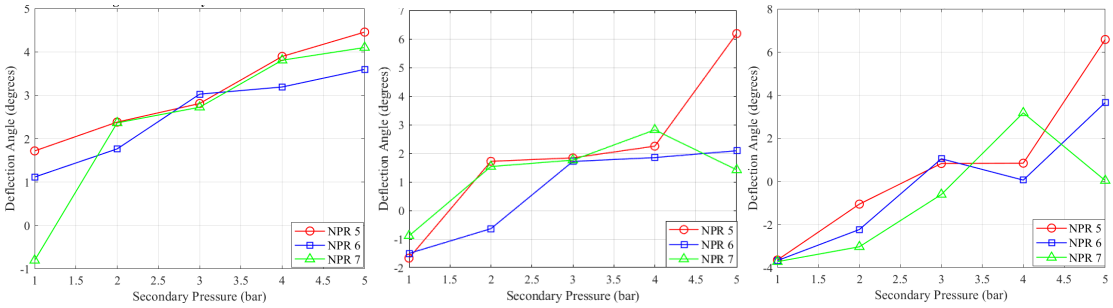

(a) Experimental (b) Simulation (ImageJ) (c) Simulation Data

Figure 4.2.1: Secondary Pressure Vs Deflection angle for various NPR at Mach 1.4

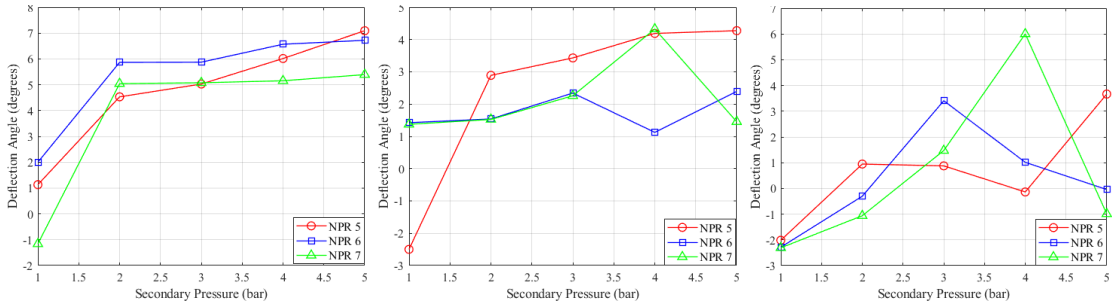

(a) Experimental (b) Simulation (ImageJ) (c) Simulation Data

Figure 4.2.2: Secondary Pressure Vs Deflection angle for various NPR at Mach 1.6

Figure 4.2.3 shows that the deflection is generally higher for Mach 1.6 compared to Mach 1.4 at every NPR at the same secondary pressure. At NPR 5, the deflection angle is increasing steadily with secondary pressure. The difference in deflection between Mach 1.4 and Mach 1.6 is not very significant at lower SPR but becomes more noticeable at higher secondary pressures and lower NPR. At NPR 6, a sharp increase in deflection can be seen at lower secondary pressures followed by a gradual increase at higher secondary pressures, for both the Mach numbers. At NPR 7, the highest deflection angles can be observed, but the rate of increase slows down at higher secondary pressures, suggesting a saturation limit, beyond which increasing the secondary pressure does not have a significant effect on deflection. The difference between Mach 1.4 and Mach 1.6 is most pronounced at this NPR, showing that higher NPRs are more effective at higher Mach numbers.

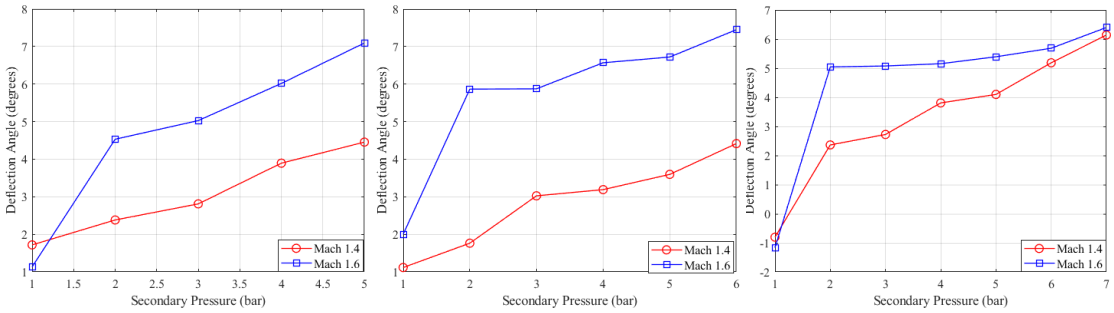

(a) NPR 5 (b) NPR 6 (c) NPR 7

Figure 4.2.3: Secondary Pressure Vs Experimental Deflection angle for Mach 1.4 and Mach 1.6 at various NPR

4.2.3. Evaluation of Results Based on First Shock Diamond Distance

Since the location of the first shock diamond affects the pressure distribution and flow expansion downstream, it directly influences the deflection angle. So, plots were drawn comparing the SPR and the distance of the first shock diamond for experimental and simulation result as shown in the Figure 4.2.3 and Figure 4.2.4. Experimental and simulation results showed different shock positions, which can explain the variation in deflection angles. The distance of the first shock diamond is generally increasing with the increase in SPR, indicating shift in shock system downstream. CFD data are significantly higher than experimental values, indicating shock is further downstream in simulations.

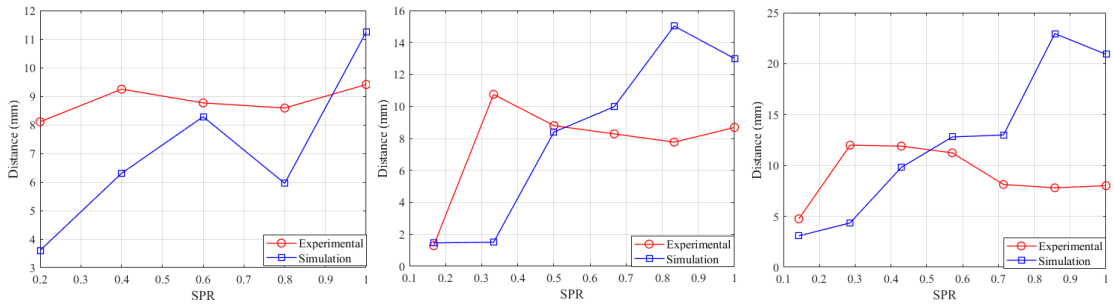

(a) NPR 5 (b) NPR 6 (c) NPR 7

Figure 4.2.4: SPR Vs Distance of first shock diamond from outlet of nozzle for Mach 1.4

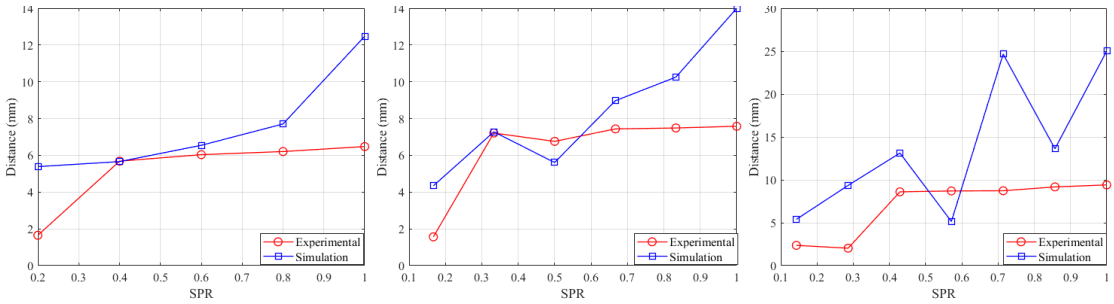

(a) NPR 5 (b) NPR 6 (c) NPR 7

Figure 4.2.5: SPR Vs Distance of first shock diamond from outlet of nozzle for Mach 1.6

4.2.4. Comparison of Experimental and Simulation Results

According to the experimental data, it can be observed that increasing the SPR positively effected the deflection angle when NPR is kept constant. However, at lower SPR values, similar trend can be observed from simlation data. Increasing SPR leads to a significant deviation in experimental and simulation results. This deviation is more pronounced at moderate SPR values and NPR 6 and 7. Additionally, this deviation is more prominent at Mach 1.6, reflecting increased deflection at higher Mach. For example, in figure 4.2.6 looking at the blue line, which is the data extracted from simulation, when NPR is 6, highest peak is obtained at 0.5 SPR, followed by a drop in deflection angle and then slowly starting to rise at SPR 0.667.

This discrepancies between experimental and simulation data could be due to some simulation not being converged and measurement error while calculating angle using imageJ. It can also be seen that experimental results are showing greater deflection angle than the simulation results. It is also interesting to note that imageJ based measurement showed a trend closer to experimental data but still very different from it. Another abnormality that can be seen is that, at NPR 7 and secondary pressure 1 bar for

both Mach 1.4 and Mach 1.6, negative deflections are observed in experimental data. Likewise, simulation results showed negative deflection at lower SPR for all NPR values. Maximum deflection angle of 7.449 degrees was obtained at SPR 1 and NPR 6 at Mach 1.6 whereas minimum deflection angle of -0.803 was obtained at SPR 0.143 and NPR 7 at Mach 1.4.

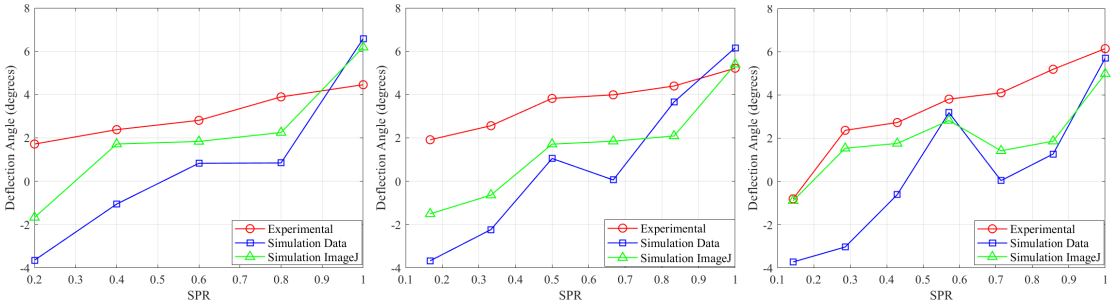

(a) 5 bar (b) 6 bar (c) 7 bar

Figure 4.2.6: SPR Vs Deflection for experimental and simulation results at Mach 1.4

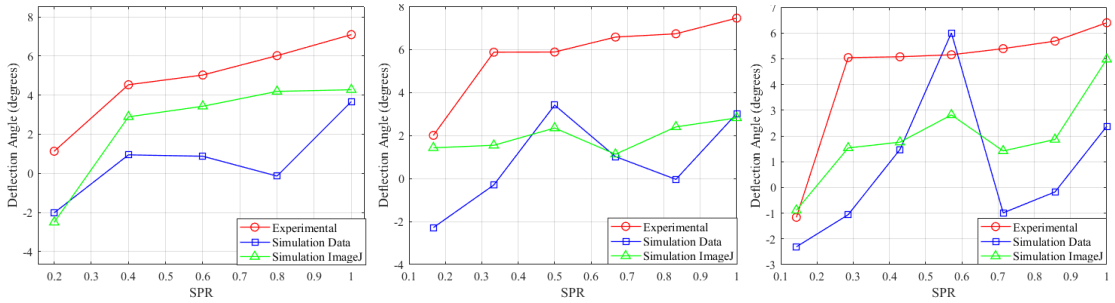

(a) 5 bar (b) 6 bar (c) 7 bar

Figure 4.2.7: SPR Vs Deflection for experimental and simulation results at Mach 1.6

4.3. Work Completed

1. Design and fabrication of nozzles for Mach 1.4 and Mach 1.6 with and without secondary inlet.

2. Numerical simulation of 2D nozzles by varying NPR and SPR.

3. Development of a fully functional setup for FTV.

4. Experimental testing of the fabricated nozzles for different NPR and SPR values, along with flow visualization of the under-expanded exhaust jet using a Z-type schlieren setup.

5. Comparison and analysis of numerical and experimental results.

4.4. Limitations

1. Limited compressor tank capacity, resulting in rapid pressure drop and short testing durations.

2. The maximum operating pressure for both compressors is 8 bar, restricting the range of NPR and SPR values for testing.

3. The surface finish and dimensional accuracy of the 3D-printed nozzles were not as smooth and precise as modeled in CAD.

4. Measurement inaccuracies while using ImageJ.

5. Limited zoom-in capability of the camera for capturing details at the nozzle outlet section.

4.5. Problems Faced

1. Leakages in fittings, valves, and connections during experimental testing.

2. The initially printed nozzle with a secondary inlet broke due to inadequate thickness and stress concentration. This was resolved by increasing the thickness and adding fillets.

3. Achieving precise glass cutting and ensuring firm adhesion to the printed nozzle was challenging.

4. Calibration and sensitivity adjustments for clear imaging using the Z-type schlieren setup were somewhat tricky.

5. Solution convergence was not achieved in some simulations, leading to unreliable results.

4.6. Budget Analysis

The estimation of the budget for this project is shown in table[4.6.1]:

Table 4.6.1: Budget Table

S.N.	Particulars	Amount(Rs.)	Remarks
1.	Sony ZV-E10 Mirror less Camera		Available in "Flow Visualization Lab" in DMAE
2.	Compressor Repair	7200	
3.	3D Printing Filament	2500	
4.	Ball Valves	800	
5.	Solenoid Valve	2000	
6.	PU Pipes	2000	
7.	PU Connectors	1020	
8.	Socket	450	
9.	Glass Cutter	400	
10.	Adhesive	350	
11.	Electronics: Power Supply Unit Toggle Switch Wires Multiplug Switches Light Source	 2000 450 250 650 150 500	
12.	Miscellaneous	3500	
	Total	24220	

CHAPTER 5:
CONCLUSION AND FUTURE ENHANCEMENT

5.1. Conclusion

The study employed a converging-diverging nozzle designed to achieve supersonic flow conditions with and without secondary flow injection to investigate Shock Vector Control (SVC) as a method of fluidic thrust vectoring. Supersonic nozzles for Mach 1.4 and Mach 1.6 were designed and fabricated, with and without secondary inlets. Numerical study was carried out using ANSYS Fluent while experimental tests were performed after the fabrication of thrust vectoring setup and visualized using Z-type schlieren setup. The study involved variation of NPR from 5 to 7 and SPR up to 1. The results demonstrated significant flow deflections influenced by secondary flow injection. The deflection angle increased on increasing the SPR. Higher deflection angles were acheived at higher Mach and higher secondary pressures. Experimental results showed maximum deflection angle of 7.449 degrees, obtained at SPR 1 and NPR 6 at Mach 1.6 whereas minimum deflection of -0.803 was obtained at SPR 0.143 and NPR 7 at Mach 1.4. Similarly, simulation results showed maximum deflection of 6.185 obtained at SPR 1 and NPR 5 at Mach 1.4 and minimum deflection of -0.638 was obtained at SPR 0.167 and NPR 6 at Mach 1.4. Deflection data obtained by post processing CFD images via imageJ were not very reliable as it neither aligned with experimental results nor with the numerical data. This could be due to human error in angle measurements, as shock intersections were not as distinct as in the experimental schlieren images. Thus, a more accurate measurement technique is necessary for calculation of deflection angle from velocity contours obtained from CFD. Moreover, maintaining consistent experimental conditions, error free angle measurements and achieving higher convergence in simulations can lead to better agreement between experimental and simulation results.

5.2. Scope for Future Enhancement

1. Resin printing can be used for nozzle fabrication to achieve better surface finish and dimensional accuracy.

2. A higher-resolution camera, improved LED lighting, and advanced image processing techniques for more accurate flow visualization and measurements.

3. Larger schlieren mirrors, better cutoffs, and the use of colored filters can further enhance the sensitivity and clarity of the schlieren imaging system.

4. Numerical simulation methods can be improved to ensure reliable solution convergence across a wider range of operating conditions.

5. Studies at higher Mach numbers can be conducted with larger compressor tanks and higher operating pressures to extend the analysis.

6. Other FTV techniques can be explored and compared with SVC, including the influence of secondary inlet location and size to gain a more comprehensive understanding of the performance characteristics.

7. To enhance the accuracy and depth of the result, 3D simulation was considered. However, 3D meshing generated significantly higher number of elements, as detailed in appendix. Due to limitations in computational time, the scope of the analysis was constrained to 2D simulation. Future work can focus on extending to a 3D simulation.

BIBLIOGRAPHY

[1] S. Maharjan, "Design and setup of z-type schlieren imaging system for flow visualization," 2023.

[2] T. Shakouchi and S. Fukushima, "Fluidic thrust, propulsion, vector control of supersonic jets by flow entrainment and the coanda effect," *Energies*, no. 1, p. 13, 2022.

[3] R. L.Yang, H.Yuan and Z. et al., "Correction to the photometric magnitudes of the gaia early data release 3," 2021.

[4] K. A. Deere, "Summary of fluidic thrust vectoring research conducted at nasa langley research center," *AIAA-2003-3800*, p. 18, June 23-26,2003.

[5] L. Kral, "Active flow control technology," *ASME Fluids Engineering Technical Brief*, 1999.

[6] K. Deere, "Pab3d simulations of a nozzle with fluidic injection for yaw thrust-vector control," *the 34th AIAA/ASME/SAE/ASEE Joint Propulsion Conference and Exhibit*, 13-15 July, 1998.

[7] H. Kowal, "Advances in thrust vectoring and the application of flow-control technology," *Can Aeronaut Space J*, 2002.

[8] A. Jimenez and D. Icaza, "Thrust vectoring system control concept," *IFAC Algorithms and Architectures for Real-Time Control*, p. 10, 2000.

[9] E. Bretscher, "Ehrenfest's character," *Nature*, vol. 228, pp. 291–92, 1970.

[10] "X-31 enhanced fighter maneuverability demonstrator-nasa," 2014.

[11] D. Katz, "The physics and techniques of infrared stealth," *Aviation Week*, 7 July 2017.

[12] J. Broadwell, "Analysis of the fluid mechanics of secondary injection for thrust vector control," *AIAA J.*, 1963.

[13] S. I. A. S. K. M. Saadia Afridi, Tariq Amin Khan 1ORCID and D. J. Kukulka, "Techniques of fluidic thrust vectoring in jet engine nozzles: A review," *Energies*, 2023.

[14] D. Wing, "Static investigation of two fluidic thrust-vectoring concepts on a two-dimensional convergent-divergent nozzle," 1994.

[15] A.-A. . Abdullah, "Fluidics thrust vectoring using co-flow method," *Al-Nahrain Journal for Engineering Sciences (NJES) Vol.20 No.1*, 2017.

[16] e. a. Banazadeh, A., ""experimental and computational investigation into the use of co-flow fluidic thrust vectoring on a small gas turbine," *The Aeronautical Journal, vol. 112, no. 1127*, 2008.

[17] G. K. B. Yagle P. J., Miller D. N. and H. J. W., "Demonstration of fluidic throat skewing for thrust vectoring in structurally fixed nozzles," *ASME. J. Eng. Gas Turbines Power*, 2001.

[18] B. B. L. Flamm J. D., Deere K. A. and J. S. K, "Design enhancements of the two-dimensional, dual throat fluidic thrust vectoring nozzle concept," *AIAA Paper No. 2006-3701*, 2006.

[19] X. J. Gu R. and G. S., "Experimental and numerical investigations of a bypass dual throat nozzle," *J. Eng. Gas Turbines Power*, 2014.

[20] J. Anderson, *Fundamentals of Aerodynamics Fifth Edition*.

[21] "Converging-diverging nozzle internal compressible flows -lesson 4."

[22] "Available: https://seitzman.gatech.edu/classes/ae3450/underoverexpandedtwo.pdf," *School of Aerospace Engineering*.

[23] S. S. Y. S. K. A. S N, M.Kalyan and R. M. Chalkapur, "Experimental investigation of fluidic thrust vectoring by shock vector control of an ideal contour nozzle," *ternational Journal of Technical Research Science*, no. 01, pp. 25–39, Jan, 2020.

[24] M. S. Bibek Gautam, Kamal Budhathoki, "Supersonic nozzle test using high pressure compressor," 2023.

[25] D. Barara, “Nozzle-design-moc,” *GitHub Repository*, 2023 Available: https://github.com/Daamanbarara/Nozzle-Design-MoC.

APPENDIX I

MOC CONTOUR

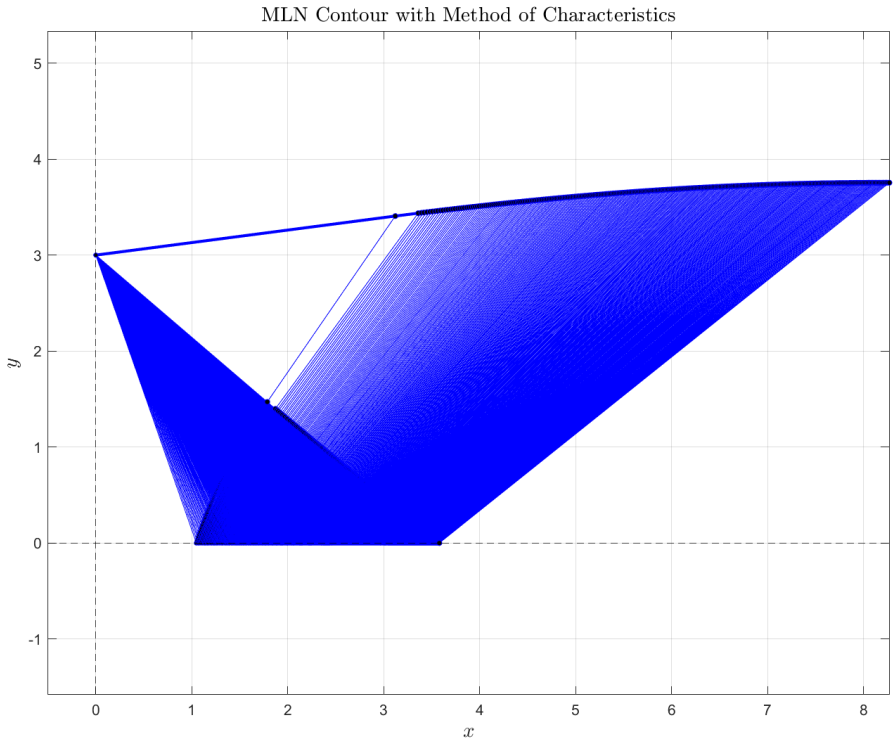

Figure A.1: Diverging section contour using MOC

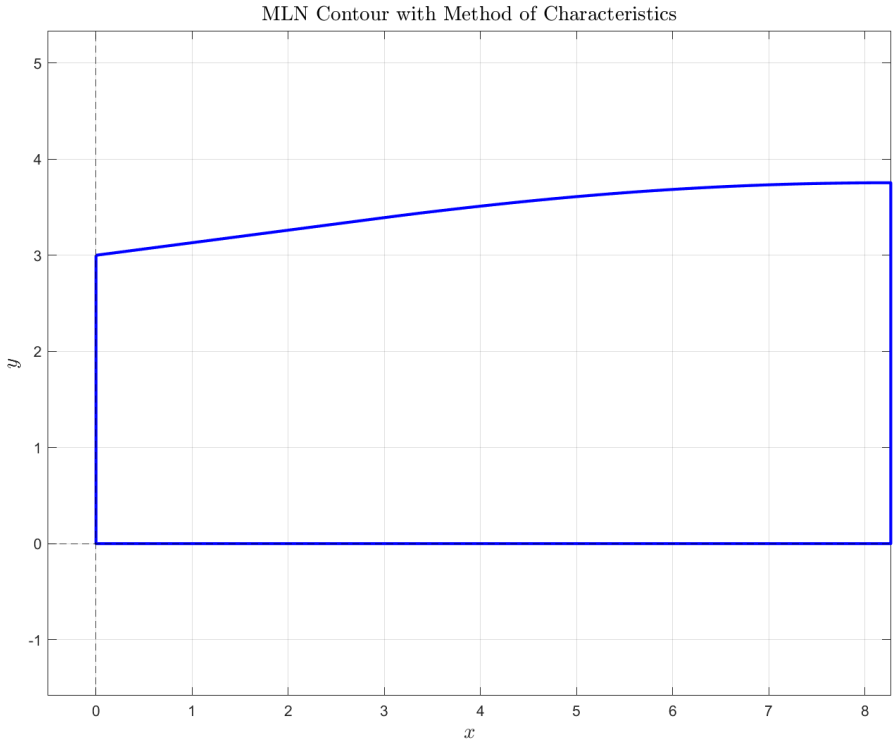

Figure A.2: Diverging section nozzle

2D SKETCH

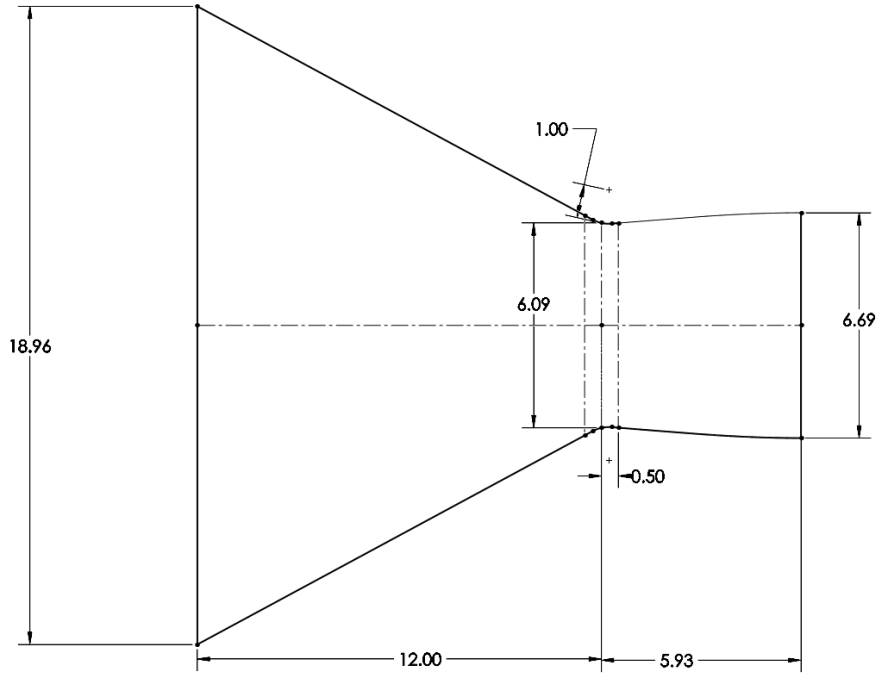

Figure A.3: 2D sketch of nozzle without secondary injection for Mach 1.4

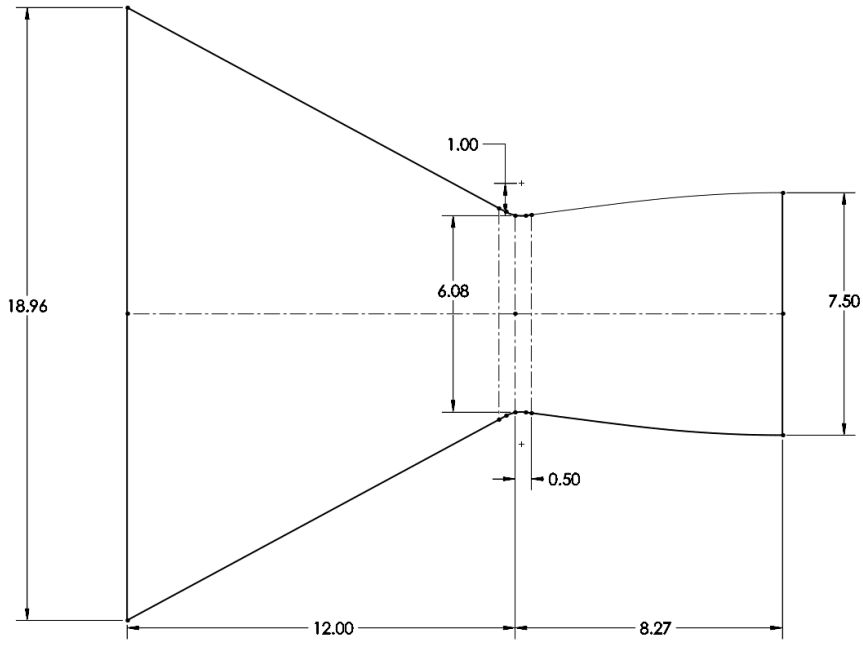

Figure A.4: 2D sketch of nozzle without secondary injection for Mach 1.6

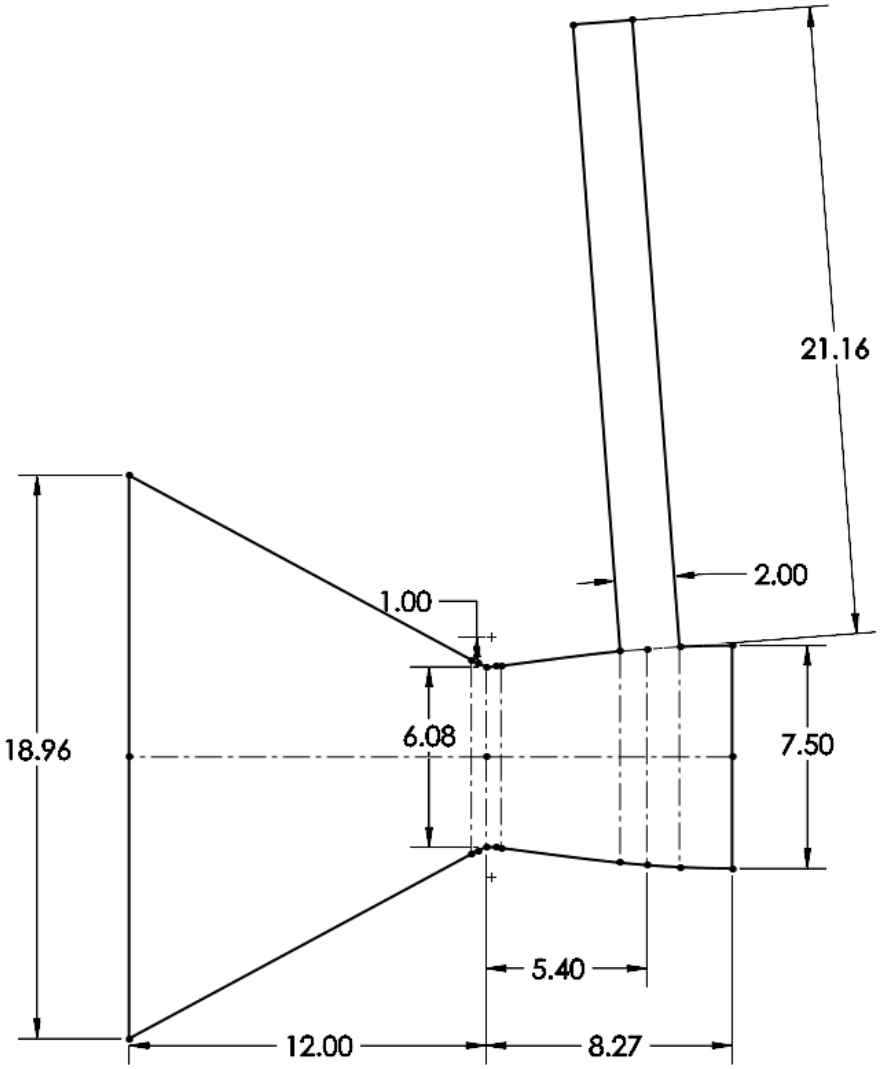

Figure A.5: 2D sketch of nozzle with secondary injection for Mach 1.6

3D GEOMETRY

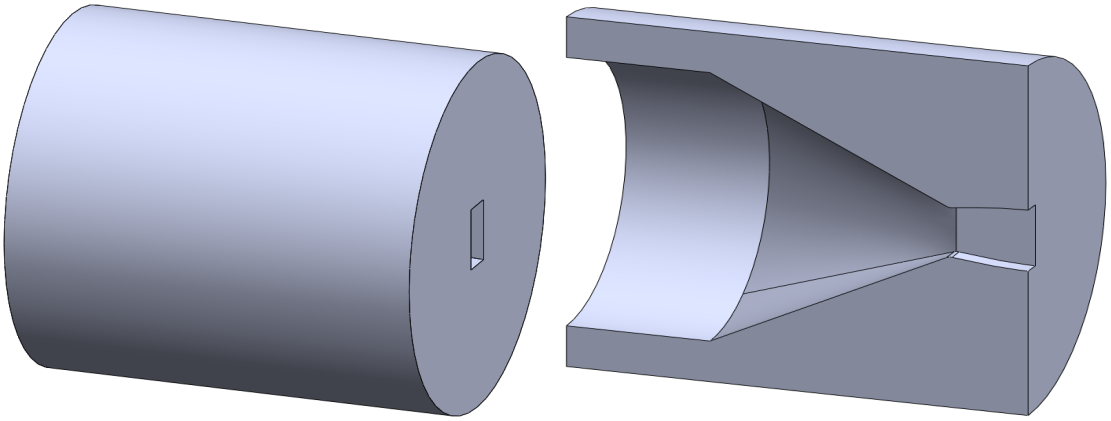

(a) 3D Geometry (b) Section view

Figure A.6: 3D geometry for Mach 1.6

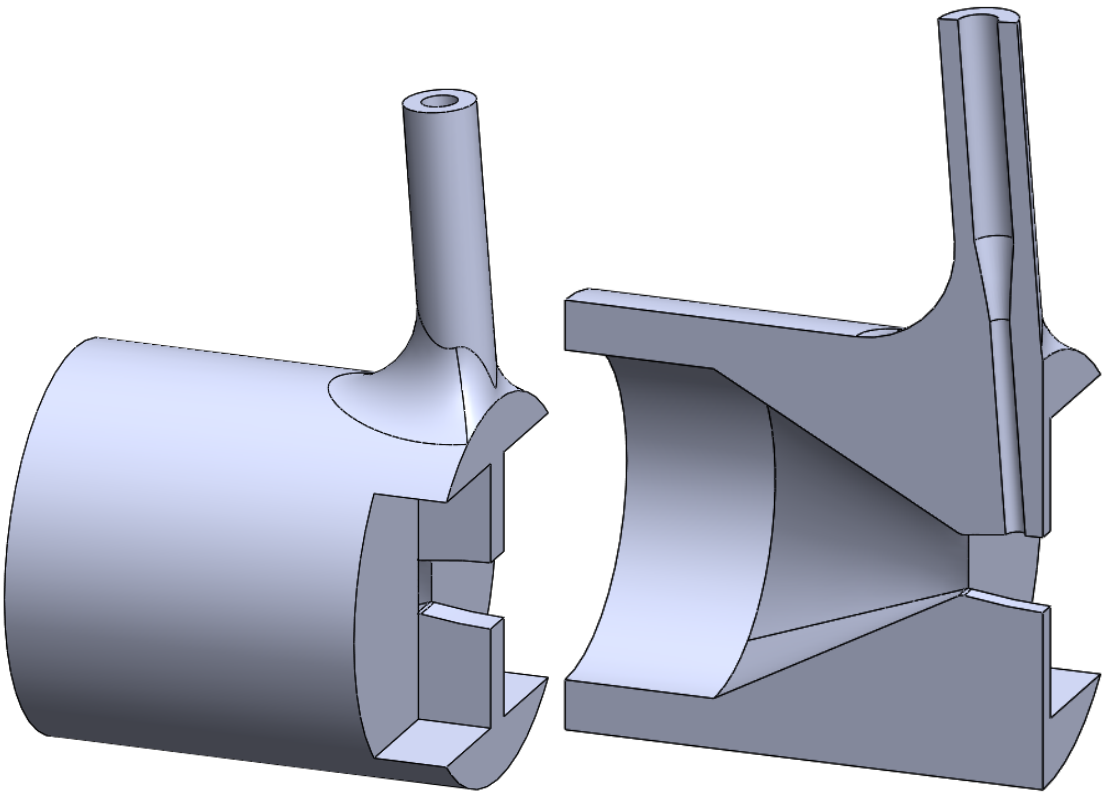

(a) 3D Geometry (b) Section view

Figure A.7: 3D geometry with secondary injection for Mach 1.6

3D Mesh

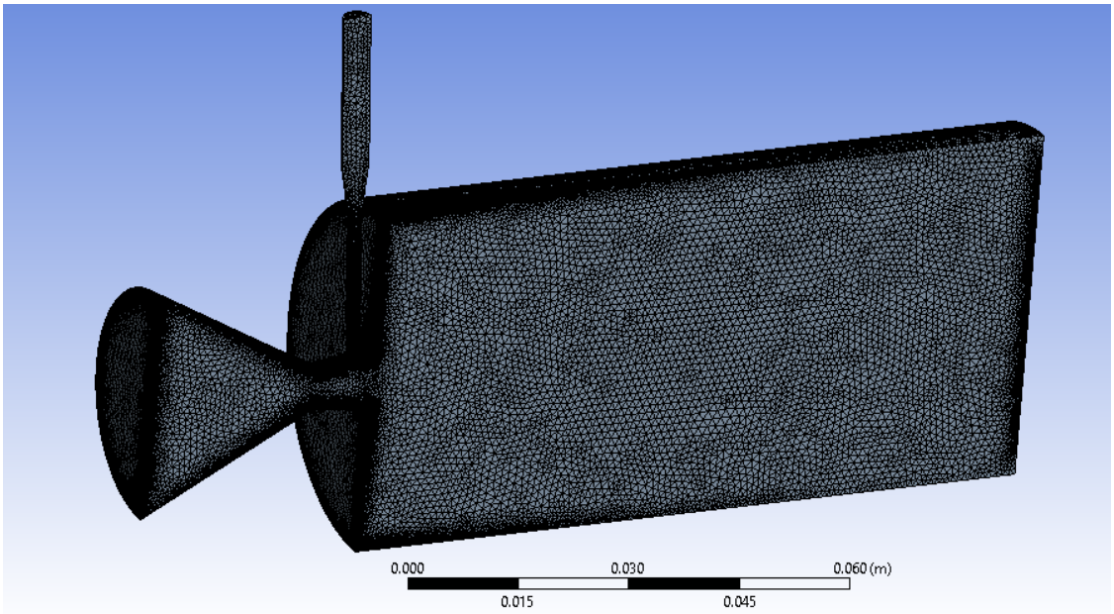

Figure A.8: 3D mesh of nozzle for Mach 1.6

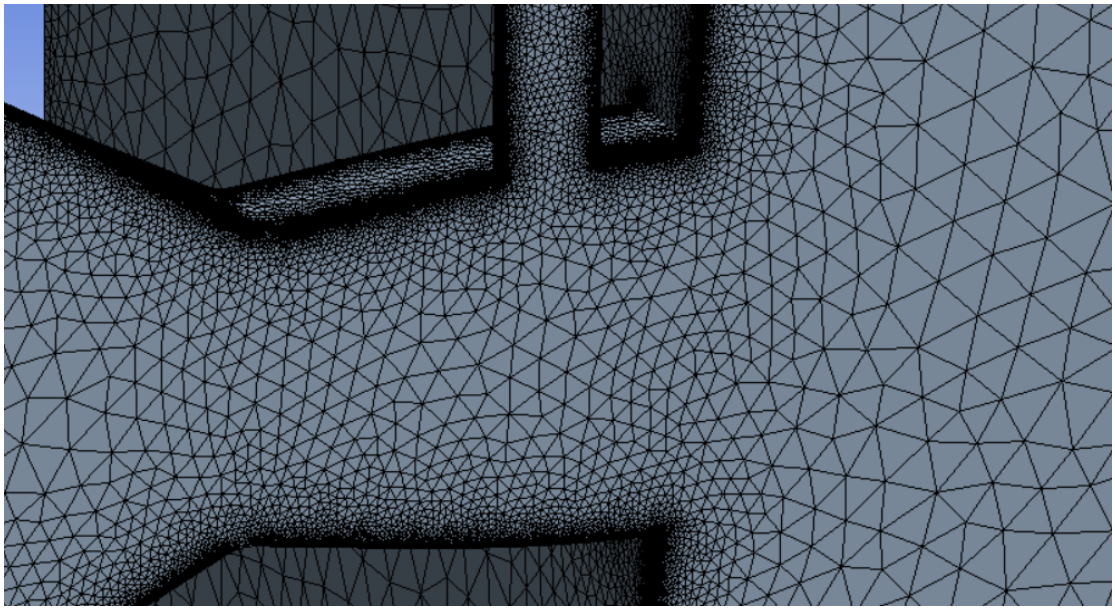

Figure A.9: Zoomed section of 3D mesh of nozzle for Mach 1.6

EXPERIMENTAL COMPONENTS

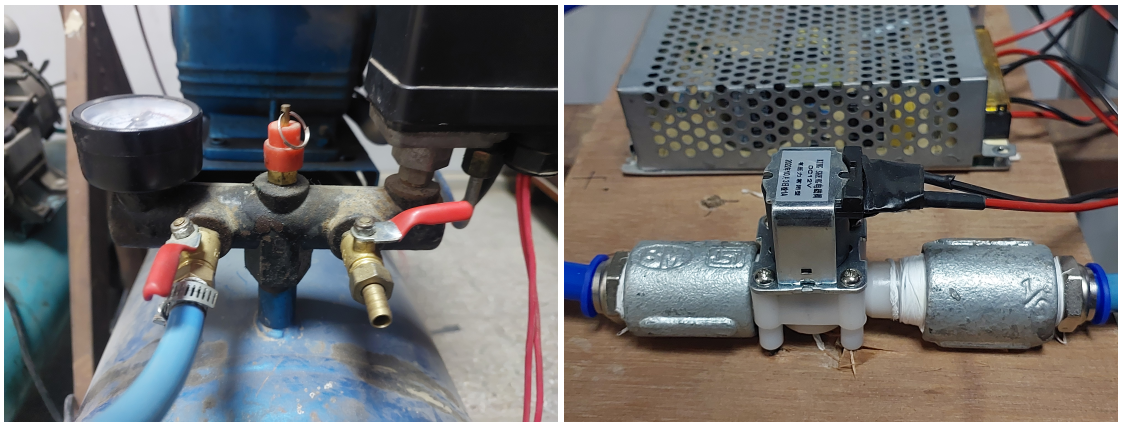

(a) Ball Valve (b) Solenoid Valve

Figure A.10: Valves

Figure A.11: Gorilla Tripod Stand

Figure A.12: Sony ZV-E10 Mirrorless Camera

MOC CODE

[25]

Listing 1: MOC MATLAB Code

```
% \begin{lstlisting}[style=cppstyle][language=Matlab, label={lst:
    arduino_code}]


Method of Characteristics Code for 2D-Minimum Length Nozzle
Author- D. Barara

clc;
clear all;
```

```
 Inputs

M_e=1.6;         % Exit Mach Number
gamma=1.4;       % Ratio of specific heats
n=300;            % Number of C_ characteristics (Right running
   characteristics)
x0=0;
y0=3;

%% Initializing arrays

nodes=(2+(n+1))*n/2;
node_no=zeros(n,1);
K_n=zeros(n,1);         % K+ constant for C+ characteristic line (left
    running)
K_p=zeros(n,1);         % K- constant for C- characteristic line (
   right running)
theta_n=zeros(n,1);     % Flow dfelection angle
nu_n=zeros(n,1);        % Prandtl Meyer function
mu_n=zeros(n,1);        % Mach angle
M_n=zeros(n,1);         % Mach number
x_n=zeros(n,1);         % X-coordinate position
y_n=zeros(n,1);         % Y-coordinate position

%% Computing Maximum wall angle and initial angle

theta_max=Prandtl_Meyer(M_e,gamma)/2;
% theta_initial=1-abs(((theta_max)-round(theta_max)));
if abs(((theta_max)-round(theta_max)))>=0.5
    theta_initial=abs(((theta_max)-round(theta_max)));
elseif abs(((theta_max)-round(theta_max)))<0.5
    theta_initial=1-abs(((theta_max)-round(theta_max)));
end
theta_delta=(theta_max-theta_initial)/(n-1);

%% Computation of variables at different nodes on the Characteristic
   lines

for j=1:n
    for i=1:n-j+1
        if j==1   % First Characteristic line
            theta_n(i,j)=theta_initial + (i-1)*theta_delta;
            nu_n(i,j)= theta_n(i,j);
            M_n(i,j)=Inverse_Prandtl_Meyer(nu_n(i,j),gamma);
            mu_n(i,j)=asind(1/M_n(i,j));
            K_n(i,j)= theta_n(i,j)+nu_n(i,j);
            K_p(i,j)= theta_n(i,j)-nu_n(i,j);
```

```
        elseif j>1  % Rest of the Characteristic data
            K_n(i,j)= K_n(i+1,j-1);
            if i==1 % Centerline
                K_p(i,j)= -1*K_n(i,j);
                theta_n(i,j)= 0;
                nu_n(i,j)= K_n(i,j);
                M_n(i,j)=Inverse_Prandtl_Meyer(nu_n(i,j),gamma);
                mu_n(i,j)=asind(1/M_n(i,j));
            else    % Internal Points (i>1)
                K_p(i,j)= K_p(i-1,j);
                theta_n(i,j)=(K_n(i+1,j-1)+K_p(i-1,j))/2;
                nu_n(i,j)=(K_n(i+1,j-1)-K_p(i-1,j))/2;
                M_n(i,j)=Inverse_Prandtl_Meyer(nu_n(i,j),gamma);
                mu_n(i,j)=asind(1/M_n(i,j));
            end
        end
    end
end

%% Coordinates Computation
% Coordinates of the charateristic line
for j=1:n
    for i=1:n-j+1
        if j==1
            if i==1
                A=((theta_n(i,j)))-((mu_n(i,j)));
                B=0;
                x_n(i,j)=(y0-tand(A)*(x0))/(tand(B)-tand(A));
                y_n(i,j)=0;
            else % (i>1) Rest of the points of First Characteristic
                line
                A=theta_n(i,j)-mu_n(i,j);
                B=((theta_n(i,j)+theta_n(i-1,j))/2)+((mu_n(i,j)+mu_n(
                    i-1,j))/2);
                x_n(i,j)=(y0-tand(A)*(x0)-y_n(i-1,j)+tand(B)*(x_n(i
                    -1,j)))/(tand(B)-tand(A));
                y_n(i,j)=(tand(B)*(x_n(i,j)-x_n(i-1,j)))+y_n(i-1,j);
            end
        elseif j>1
            if i==1 % Centerline
                A=((theta_n(i+1,j-1)+theta_n(i,j))/2)-((mu_n(i+1,j-1)
                    +mu_n(i,j))/2);
                B=0;
                x_n(i,j)=(y_n(i+1,j-1)-tand(A)*(x_n(i+1,j-1)))/(tand(
                    B)-tand(A));
                y_n(i,j)=0;
            else %(i>1) Rest of the points
```

```
                A=((theta_n(i+1,j-1)+theta_n(i,j))/2)-((mu_n(i+1,j-1)
                    +mu_n(i,j))/2);
                B=((theta_n(i-1,j)+theta_n(i,j))/2)+((mu_n(i-1,j)+
                    mu_n(i,j))/2);
                x_n(i,j)=(y_n(i+1,j-1)-tand(A)*(x_n(i+1,j-1))...
                    -y_n(i-1,j)+tand(B)*(x_n(i-1,j)))/(tand(B)-tand(A
                        ));
                y_n(i,j)=(tand(B)*(x_n(i,j)-x_n(i-1,j)))+y_n(i-1,j);
            end
        end
    end
end
% Initializing array for coordinates of the wall nodes
x_wall=zeros(1,n+1);
y_wall=zeros(1,n+1);
theta_wall=zeros(1,n+1);

% Point 'A' at the expansion point
x_wall(1,1)=x0;
y_wall(1,1)=y0;
theta_wall(1,1)=theta_max;

% Computation of the coordinates of rest of the wall nodes
for j=2:n+1
    if j==2
        A=(theta_wall(1,1));
        B=((theta_n(n-j+2,j-1)))+((mu_n(n-j+2,j-1)));
        x_wall(1,j)=(y_wall(1,j-1)-tand(A)*(x_wall(1,j-1))...
            -y_n(n-j+2,j-1)+tand(B)*(x_n(n-j+2,j-1)))/(tand(B)-tand(A
                ));
        y_wall(1,j)=tand(theta_wall(1,1))*(x_wall(1,j)-x_wall(1,j-1))
            +y_wall(1,j-1);
    elseif j>2
        A=(theta_n(n-j+3,j-2)+(theta_n(n-j+2,j-1)))/2;
        B=((theta_n(n-j+2,j-1))+(mu_n(n-j+2,j-1)));
        x_wall(1,j)=(y_wall(1,j-1)-tand(A)*(x_wall(1,j-1))...
            -y_n(n-j+2,j-1)+tand(B)*(x_n(n-j+2,j-1)))/(tand(B)-tand(A
                ));
        y_wall(1,j)=tand(A)*(x_wall(1,j)-x_wall(1,j-1))+y_wall(1,j-1)
            ;
    end
end

%% Plotting of the nozzle contour and characteristic lines
figure(1)
plot(x_wall,y_wall,'b-','LineWidth',2)
yline(0,'k--');
```

```
xline(0,'k--');
grid on
hold on
% Plotting the C- Characteristics from 'a' to points on First
   Characteristic line
for j=1:n
 plot([x0 x_n(j,1)],[y0 y_n(j,1)],'b-o','MarkerFaceColor','k','
    MarkerSize',3)
end
% Plotting the C+ Characteristics
for j=1:n-1
     plot(x_n(1:n-j+1,j),y_n(1:n-j+1,j),'b-o','MarkerFaceColor','k','
        MarkerSize',3)
end
% Plotting and connecting the Inner nodes
 for j=1:n
    for i=2:n-j+1
        plot([x_n(i,j) x_n(i-1,j+1)],[y_n(i,j) y_n(i-1,j+1)],'b-o','
           MarkerFaceColor','k','MarkerSize',3)
    end
 end
% Joining the C+ Characteristics with Wall nodes
for i=2:n+1
        plot([x_wall(1,i) x_n(n-i+2,i-1)],[y_wall(1,i) y_n(n-i+2,i-1)
           ],'b-o','MarkerFaceColor','k','MarkerSize',3.5)
end

title('MLN␣Contour␣with␣Method␣of␣Characteristics','fontsize',14,'
   interpreter','latex')
xlabel('$x$','fontsize',14,'interpreter','latex')
ylabel('$y$','fontsize',14,'interpreter','latex')
xlim([x0-0.5 max(x_wall)])
ylim([y0-1.0 max(y_wall)])
axis equal

%% Writing the Data points of the MLN Contour
x_contour_data= [x_wall max(x_wall) 0 x_wall(1,1)];
y_contour_data= [y_wall 0 0 y_wall(1,1)];
num=length(x_contour_data);
z_contour_data=zeros(1,num);
Group_num=ones(1,num).*2;
a=1:num;
data=[x_wall;y_wall;zeros(1,length(x_wall))];
file=fopen('MLN_Contour_Soliworks_Data.txt','w');
fprintf(file,'%d␣%d␣%d\n',data);
fclose(file);

```

```
% Plot with Nozzle Datapoints
figure(2)
plot(x_contour_data,y_contour_data,'b-','LineWidth',2)
yline(0,'k--');
xline(0,'k--');
grid on
title('MLN Contour with Method of Characteristics','fontsize',14,'
    interpreter','latex')
xlabel('$x$','fontsize',14,'interpreter','latex')
ylabel('$y$','fontsize',14,'interpreter','latex')
xlim([x0-0.5 max(x_wall)])
ylim([y0-1.0 max(y_wall)])
axis equal
```